

2

Original contains color plates; all other reproductions will be in black and white

DTIC
S ELECTE D
FEB 3 1993
C

ARMY RESEARCH LABORATORY



AD-A259 799



Reacting Liquid Monopropellant Sprays—Experiments With High Velocity Full Cone Sprays in 33 MPa, 500° C Nitrogen

Avi Birk
Michael McQuaid
Gary Bliesener

ARL-TR-17

December 1992

APPROVED FOR PUBLIC RELEASE; DISTRIBUTION IS UNLIMITED.

93 2 2 003

93-01891



63pk

NOTICES

Destroy this report when it is no longer needed. DO NOT return it to the originator.

Additional copies of this report may be obtained from the National Technical Information Service, U.S. Department of Commerce, 5285 Port Royal Road, Springfield, VA 22161.

The findings of this report are not to be construed as an official Department of the Army position, unless so designated by other authorized documents.

The use of trade names or manufacturers' names in this report does not constitute indorsement of any commercial product.

REPORT DOCUMENTATION PAGE

Form Approved
OMB No. 0704-0188

Public reporting burden for this collection of information is estimated to average 1 hour per response, including the time for reviewing instructions, searching existing data sources, gathering and maintaining the data needed, and completing and reviewing the collection of information. Send comments regarding this burden estimate or any other aspect of this collection of information, including suggestions for reducing this burden, to Washington Headquarters Services, Directorate for Information Operations and Reports, 1215 Jefferson Davis Highway, Suite 1204, Arlington, VA 22202-4302, and to the Office of Management and Budget, Paperwork Reduction Project (0704-0188), Washington, DC 20503.

1. AGENCY USE ONLY (Leave blank)		2. REPORT DATE December 1992	3. REPORT TYPE AND DATES COVERED Final, Feb 90 - Feb 92	
4. TITLE AND SUBTITLE Reacting Liquid Monopropellant Sprays—Experiments With High Velocity Full Cone Sprays in 33 MPa, 500° C Nitrogen			5. FUNDING NUMBERS 44592-201-11-4601	
6. AUTHOR(S) Avi Birk, Michael McQuaid, and Gary Bliesener				
7. PERFORMING ORGANIZATION NAME(S) AND ADDRESS(ES)			8. PERFORMING ORGANIZATION REPORT NUMBER	
9. SPONSORING / MONITORING AGENCY NAME(S) AND ADDRESS(ES) U.S. Army Research Laboratory ATTN: AMSRL-OP-CI-B (Tech Lib) Aberdeen Proving Ground, MD 21005-5066			10. SPONSORING / MONITORING AGENCY REPORT NUMBER ARL-TR-17	
11. SUPPLEMENTARY NOTES				
12a. DISTRIBUTION / AVAILABILITY STATEMENT Approved for public release; distribution is unlimited.			12b. DISTRIBUTION CODE	
13. ABSTRACT (Maximum 200 words) Experiments were conducted to elucidate the jet breakup, atomization, and combustion of liquid monopropellant sprays through the use of imaging and spectroscopic techniques. Hydroxylammonium nitrate (HAN) based monopropellants LGP1845 and LGP1898 were injected at velocities ranging from 100 to 240 m/s through circular orifices into 33-MPa 500° C nitrogen. Experiments with nitromethane, ethanol, and aqueous HAN and TEAN solutions were also conducted. Spray dynamics were recorded via high-speed cinematography. Breakthroughs in the imaging of combusting sprays were achieved by side illumination of the sprays with pulsed laser light sheets, and by seeding the propellants with nitrate salts of sodium or lithium to enhance flame luminosity. Emission spectroscopy was used to identify combustion intermediates and their relative contribution to color content in the cinematic images. Temperature measurements at the center of the sprays provided additional information regarding spray structures and reactivities. In the experiments reported here, sprays ignite in the far field and flame advances upstream sustained by extensive turbulent gas recirculation in the closed chamber. The experiments reveal the presence of large liquid drops as well as intense, random burning in vortices. The experiments with nitromethane and ethanol indicate that the dynamic behavior of sprays change when the ambient temperature and pressure exceed critical values. The experimental results are discussed in the context of understanding and modeling spray combustion phenomena in regenerative liquid propellant guns.				
14. SUBJECT TERMS injectors; liquid atomization; spray combustion; supercritical combustion; color image analysis; emission spectroscopy; regenerative liquid propellant guns; liquid gun propellants			15. NUMBER OF PAGES 69	
			16. PRICE CODE	
17. SECURITY CLASSIFICATION OF REPORT UNCLASSIFIED	18. SECURITY CLASSIFICATION OF THIS PAGE UNCLASSIFIED	19. SECURITY CLASSIFICATION OF ABSTRACT UNCLASSIFIED	20. LIMITATION OF ABSTRACT UL	

INTENTIONALLY LEFT BLANK.

TABLE OF CONTENTS

	<u>Page</u>
LIST OF FIGURES	v
LIST OF TABLES	vi
PREFACE	vii
1. INTRODUCTION	1
2. EXPERIMENTAL SETUP	3
3. IMAGE DIGITIZATION AND PROCESSING	6
4. TEST MATRIX	6
5. TEMPERATURE AND PRESSURE PROFILES	8
6. SPECTROSCOPIC RESULTS	10
7. PHOTOGRAPHIC OBSERVATIONS AND ANALYSIS	12
7.1 General Observations	12
7.2 Comparative Spray Dynamics	17
7.2.1 Combustion Intensity vs. Orifice Diameter	17
7.2.2 HAN vs. LGP1845 Spray Dynamics	19
7.2.3 HAN vs. TEAN Spray Dynamics	19
7.2.4 LGP1845 vs. LGP1898 Spray Dynamics	23
7.2.5 Water Sprays	23
7.2.6 Supercritically Evaporating Sprays	31
7.2.7 Spray Combustion of LGP1845/Nitromethane Sprays	31
7.2.8 High Injection Velocity Sprays	35
8. COLOR IMAGE PROCESSING AND ANALYSIS	35
9. DISCUSSION	45
9.1 Liquid Jet Breakup and Spray Formation	45
9.1.1 Spray Divergence Angle	48
9.1.2 Breakup Length	50
9.1.3 Primary Drop Size Distributions	51
9.2 Secondary Atomization and Droplet Coalescence	52
9.3 Thermal Considerations—Heat Transfer, Evaporation, and Combustion	53
9.4 Implications of the Present Work to Modeling of Combustion in Guns	56

	<u>Page</u>
10. CONCLUSIONS	58
11. REFERENCES	61
APPENDIX: COLOR IMAGE PROCESSING	65
LIST OF SYMBOLS	69
DISTRIBUTION LIST	71

LIST OF FIGURES

<u>Figure</u>	<u>Page</u>
1A. Schematic of Experimental Setup	4
1B. Photograph of Experimental Setup	4
2. Chamber Pressure and Temperatures vs. Time for HAN-Based Propellants	9
3. Chamber Pressures for Three Different Jet Sizes	10
4. Emission Spectra of Unseeded LGP1845	11
5. Emission Spectra of LGP1898 Seeded with LiNO_3	12
6. Video Pictures of 0.5-mm LGP1845 Jet (Test No. 1)	13
7. Video Pictures of 2.0-mm LGP1845 Jet (Test No. 5)	13
8. Video Pictures of 0.5-mm Jets of HAN and LGP1845 (Test Nos. 23 and 15)	15
9. Cine Pictures of HeNe Beam Through Test Section (Test No. 12)	19
10. Cinematic Sequence of HAN Spray (2,000 frames/s, Test No. 23)	21
11. Cinematic Sequence of TEAN Spray (2,000 frames/s, Test No. 24)	21
12. Cinematic Sequence of 0.5-mm LGP1845 (2,000 frames/s, Test No. 15)	25
13. Cinematic Sequence of 0.5-mm LGP1898 (2,000 frames/s, Test No. 19)	25
14. Cinematic Sequences of Flames of 0.5-mm LGP1845 and LGP1898 (2,000 frames/s, Test Nos. 13 and 20)	27
15. Intensity Histogram of LGP1845 Flame (Test No. 13)	27
16. Intensity Histogram of LGP1898 Flame (Test No. 20)	29
17. Cinematic Sequence of 1-mm Evaporating Water Sprays (5,000 frames/s, Test No. 26)	29
18. Supercritical evaporation, 0.5-mm Nitromethane (Test No. 32) and 1-mm Ethanol (Test No. 34)(Sequences at 5,000 frames/s)	33
19. A 1.8-ms Sequence of Supercritically Evaporating 1-mm Ethanol Jet Demonstrating High Degree of Structural Fluctuation (Test No. 31)	33

<u>Figure</u>	<u>Page</u>
20. Cinematic Sequence of 0.5-mm LGP1845/Nitromethane Jet (5,000 frames/s, Test No. 33)	37
21. High Injection Velocity Tests With 0.5-mm Jets of LGP1845 and LGP1898 (Test Nos. 17 and 21)	37
22. Cinematic Sequence of Progression of 1-mm LGP1845 Reactants From Ignition to Quasisteady Behavior (Every 3 ms, Test No. 29)	41
23. Color Image Analysis of Figure 22 Sequence: Blue - Nonreactant Liquid; Green, Red, Yellow - Increasing Degrees of Reactivity	41
24. Cinematic Sequence of 1-mm LGP1845 Quasisteady Combustion (5,000 frames/s, Test No. 29)	43
25. Color Image Analysis of Figure 24 Sequence	43
26. The High Pressure Spray as the Counterpart of a Single-Phase Turbulent Jet	47

LIST OF TABLES

<u>Table</u>	<u>Page</u>
1. Text Matrix of Experimental Parameters and Diagnostic Techniques	7
2. Film Response to Prevalent Wavelengths in Burning Spray Illuminated by Copper Vapor Laser	39
3. Summary of Test Conditions Related to Atomization	49
4. Estimated Spray Attributes	49
5. Critical Drop Size and Secondary Breakup Times for LGP1845	54

PREFACE

The U.S. Army Ballistic Research Laboratory was deactivated on 30 September 1992 and subsequently became a part of the U.S. Army Research Laboratory (ARL) on 1 October 1992.

DTIC QUALITY INSPECTED 3

Accession For	
NTIS ORNL	<input checked="" type="checkbox"/>
DTIC TAB	<input type="checkbox"/>
Unannounced	<input type="checkbox"/>
Justification	
By	
Distribution/	
Availability Codes	
Avail and/or	
Dist	Special
A-1	23

INTENTIONALLY LEFT BLANK.

1. INTRODUCTION

The current design approach (Concept VIC) for utilizing liquid monopropellants in gun applications involves the high velocity regenerative injection of propellant from a reservoir into the combustion chamber. Experimental gun fixtures utilizing this concept have been successfully built and fired in sizes ranging from 30 to 155 mm. The experimental data obtained from these fixtures have been simulated using interior ballistic models based on a lumped parameter treatment of the combustion process (Coffee 1988; Coffee, Wren, and Morrison 1989, 1990; Wren, Coffee, and Morrison 1990). Good agreement between the experimental data and the simulations has been achieved with respect to pressure-time histories, piston motions, and projectile velocity. Despite this success, more fundamental characterization and modeling of Regenerative Liquid Propellant Gun (RLPG) processes is required for predicting high-performance gun firings and resolving remaining technical issues.

One technical issue which has received considerable attention is the large pressure fluctuations observed in virtually every RLPG caliber and geometry tested to date (Graham 1988, Knapton 1990, Watson 1989). Although muzzle velocity is little affected by these fluctuations, there is concern that they may have an adverse effect on projectile components. Analysis of pressure vs. time traces from 155-mm gun firings reveals that the fluctuations have both coherent and incoherent wave structure, with most of the energy stored in the incoherent waves (Haberl 1992). The coherent waves can, in most cases, be related to acoustic modes which depend on the global geometry of the combustion chamber. The source of incoherent fluctuations is uncertain. Attempts to reduce or eliminate pressure fluctuations guided by analysis of experimental gun firing data have been only partially successful. Some reduction of the coherent fluctuations has been achieved through the use of baffles and cavities (Watson, Knapton, and Boyer 1989), jet dispersion devices (DeSpirito et al. 1991), and modified injector faces (Watson, Knapton, and Boyer 1989). Recently, fluctuations were eliminated entirely in the Ballistic Research Laboratory (BRL) 30-mm RLPG fixture by inserting a rubber hose in the combustion chamber (Boyer 1992). However, the reason this device works is not understood; and the implementation and usefulness of such a device in larger, higher performance guns such as the 120-mm tank gun or the 155-mm howitzer remain to be proven.

Whether coherent or incoherent, pressure fluctuations will be eliminated if the volume of unreacted propellant present in the combustion chamber at any instant is reduced sufficiently. Realistic two-phase flow modeling of gun combustion processes would suggest approaches to achieving this goal. However, experimental data concerning the dispersion patterns of liquid in the chamber and actual volumetric

combustion rates are required to validate such models. Experimental visualization of spray combustion has proven useful in obtaining such information for a variety of applications, and several studies related to RLPGs have been reported. Baier (1986) attempted to visualize spray dynamics and combustion in an actual gun fixture, but the phenomena of interest were largely obscured by excess luminosity and the optically thick combustion products. To overcome the obstacles to visualizing sprays in a gun, early laboratory scale experiments with liquid gun propellant (LGP) sprays in windowed test chambers were conducted by Birk (Birk and Reeves 1987) and later by Lee (Lee et al. 1990). In both efforts, LGP1846 was injected at velocities of 50 to 100 m/s into a post-combustion environment of argon/hydrogen/oxygen (Birk and Reeves 1987) or nitrogen/methane/air (Lee et al. 1990). Both groups also used high-speed cinematography in the range of 1,000 to 5,000 frames/s with backlighting (shadowgraphy) to record events. The ambient gas temperature achieved in these experiments was close to the flame temperature of the LGP. However, observations were limited to pressures less than 9 MPa because at higher pressures radiation from the ambient gas obscured spray details. Also, fogging of the windows by the presence of water vapor and the cooling of the ambient gas by heat losses to the walls limited test durations to a few tens of milliseconds.

The photographic data of Birk (Birk and Reeves 1987) prompted Lee (Lee et al. 1988) to model the LGP sprays using the locally homogeneous flow (LHF) approximation of multiphase flow theory. Later, Lee and Faeth (Lee and Faeth 1992) concluded from their own experiments that separated flow considerations for LGP sprays must be taken into account. Although the theories yielded spray penetration distances in reasonable agreement with the experiments, the assumptions and choice of empirical constants used are suspect. Also, neither the experimental results nor the theories provide insight with respect to the pressure fluctuations observed in actual gun fixtures.

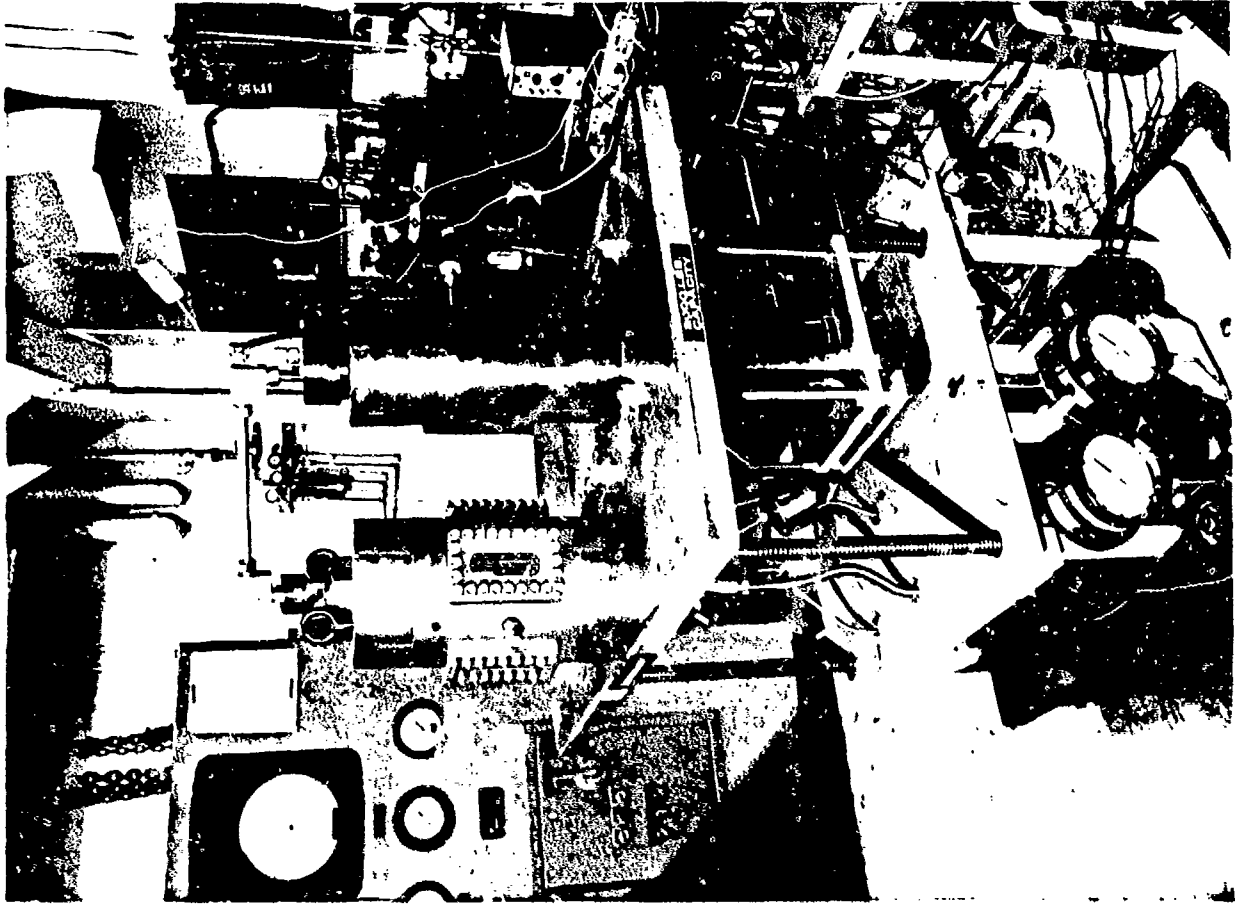
This report summarizes experiments conducted at the BRL Spray Research Facility to visualize jet breakup, atomization, and combustion of LGP sprays at pressures significantly above those studied previously. Obscuration of spray details due to radiation from the ambient gas was avoided by initiating spray reactivity (i.e., evaporation, ignition, and combustion) in 33-MPa 500° C clear nitrogen. In addition, the LGPs were seeded with lithium and/or sodium nitrate to enhance flame visibility. To avoid problems inherent in using shadowgraphic techniques, and to provide better distinction between flame and unreacted liquid particles, a copper vapor laser strobe was used to slice the spray at 90° to the camera. This allowed true color high-speed cinematography to be used for visualization, and facilitated innovative color image analysis for spatially mapping spray reactivity. Combusting sprays of LGP1845, aqueous solutions of its

subcomponents HAN and TEAN, and a newly formulated HAN-based propellant (LGP1898) which has DEHAN instead of TEAN as the fuel component (Klein et al. 1991) were investigated. Purely evaporating sprays of nitromethane and ethanol at temperatures and pressures above their critical points were also studied. The results of the experiments with the highly reactive LGP1898 were the first to detail its combustion in a spray, and they have motivated further testing of the propellant in actual gun fixtures. The experimental results are analyzed and discussed with respect to the aerodynamic theory of jet breakup. The implications of the results for modeling RLPG phenomena are also discussed.

2. EXPERIMENTAL SETUP

The experimental setup is shown schematically and pictorially in Figures 1A and 1B, respectively. Propellant is injected upward into hot nitrogen delivered to the test chamber from a high-pressure gas reservoir via a particle bed heater (PBH). The injector is a patented design based on a regenerative concept (Birk and Bliesener 1991). Injector piston motion is monitored by a Wolff Hall-effect magnetic sensor, and by a photo-interrupter device (Birk and Reeves 1987) from which the injection velocity can be determined. The PBH (Birk and Reeves 1988) is a pressure vessel which contains 1,000 cm³ of 800- μ m alumina particles. The particles fill the annular void between two porous cylindrical frits. Prior to a test, the particles are heated electrically to about 850° C. Gas is heated as it passes radially inward through the bed. The test chamber is cylindrical with a 75-mm inside diameter and a total volume of 1,050 cm³. It has four opposing 25-mm-thick rectangular sapphire windows with 97-mm \times 32-mm apertures. Chamber pressure is measured with a pressure transducer (P) (Kistler, Model 607C). The pressure regulator (PR) upstream of the PBH maintains a (preset) minimum pressure in the test chamber. System valving is controlled electropneumatically. The temperature at the center of the chamber is measured with a 0.05-mm chromel/alumel thermocouple (TC). Access and support for the thermocouples are provided by chromel and alumel electrodes fed through fittings on opposite sides of the chamber.

For the experiments reported here the injector was loaded with 35 cm³ of propellant. Among the propellants studied were LGP1845, LGP1898, aqueous solutions of HAN and TEAN, and nitromethane. Experiments with ethanol and pure water were also conducted. A small amount of water (0.5 to 0.7 cm³) was loaded between the propellant and the injection orifice to prevent the propellant from being ignited prior to injection by heat transfer from the ambient gas. (Thus, the injection of the buffer water preceded the actual propellant injection.) To flush the system after the propellant was injected, 47 cm³ of water was also loaded "behind" the propellant. The two (water) buffer zones in the injector were isolated from



NOTE: Particle bed heater is the cylinder to the right of the windowed chamber.
 Figure 1B. Photograph of Experimental Setup.

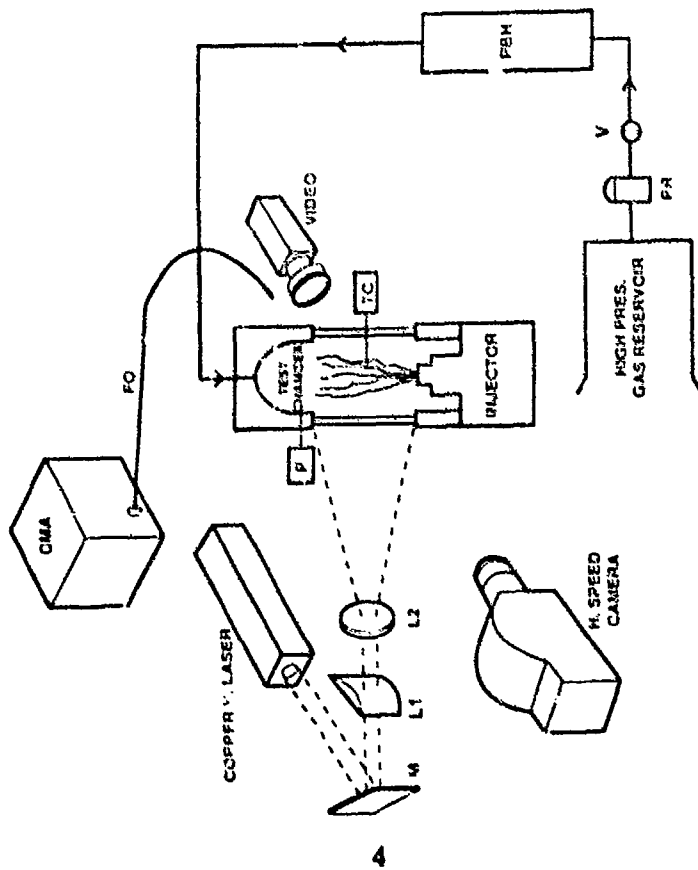


Figure 1A. Schematic of Experimental Setup.

the propellant by traveling seals. In most tests, the propellants were seeded with approximately 0.5 cm^3 of a saturated nitrate salt solution to produce flame enhancement and spectroscopic markers. Aqueous $\text{Sr}(\text{NO}_3)_2$, $\text{Ba}(\text{NO}_3)_2$, LiNO_3 , and NaNO_3 solutions were tested for these purposes. Each is fully miscible with the HAN-based propellants and it was considered that their impact on propellant chemistry and combustion would be minimal.

The propellants were typically injected into 500°C 33-MPa nitrogen. These were the highest temperature and pressure conditions that could be reliably sustained. The upper limit for pressure was the threshold above which the sapphire windows, though rated for 65-MPa service, were prone to fail. The temperature in the chamber was limited by the temperature to which the particle bed could be heated and heat losses. For safety purposes, and also for stabilizing the temperature in the test chamber, the chamber gas was continually exhausted via a 1-mm orifice (far) downstream of the chamber. This resulted in motion of the ambient gas in the chamber from the top to bottom at approximately 6-cm/s—a value much lower than the velocities characterizing the spray's dynamics. Thus, it is not a factor in the evaluation of the experimental observations.

In an attempt to achieve complete burning of propellant sprays within the field of view, and to provide maximum test duration, propellants were typically injected through a small (0.5-mm-diameter) circular orifice. Tests utilizing 1.0-mm and 2.0-mm-diameter orifices were also conducted. All injector nozzles had cylindrical exit channels with rounded inlets and a length to diameter ratio (l/d_o) equal to 4. A stem valve incorporated into the injector design sealed the orifice prior to injection. The stem valve prevented splashing and, together with the buffer water, prevented hot chamber gases from entering the injector and prematurely igniting the propellant.

For visualization, both a color video camcorder (Quasar, Model VM-21) and a high-speed framing camera (Photonic Systems, Photec IV) were used. A 10-W copper vapor laser (Oxford Lasers, Model CU10) served as a strobe. (The copper vapor laser radiates at 510.6 nm (green) and 578.2 nm (yellow) with the 510.6-nm line approximately twice as intense as the 578.2-nm line.) The laser pulses, which have a duration of 25 ns, were synchronized to the framing rate of the high-speed camera. The framing rate was typically set to either 2,000 or 5,000 frames/s. The camcorder, which runs at 60 frames/s (only), was operated in its high-speed shutter mode (1-ms exposure). The laser's 25-mm-diameter beam was optically steered by a mirror (M), cylindrical lens (L1), and a concave lens (L2) to provide a 3-mm-thick planar light sheet that sliced the chamber volume symmetrically along the cylinder axis and at 90° to the cameras.

In some tests, an EG&G strobe employing a xenon flash tube was used to backlight the jet through a diffuser. The flashes from this strobe were also triggered by the high-speed camera.

Spectroscopic measurements were made with an optical multichannel analyzer (Princeton Instruments, Model ST-1000) coupled to a monochromator (ISA Instruments, Model HR-20). A 1-m-long quartz fiber optic (FC) was used for light collection. Measurements were limited to recording emission spectra of the combustion process. The spectra were collected from a region subtending a 25-mm circle of the spray approximately 50-mm downstream of the injector—the region of highest flame intensity. Scan rate (integration) cycles of 4 or 5 ms were used. A 150-groove/mm grating was used to observe spectral ranges of approximately 500 nm. A 600-groove/mm grating, resulting in a 125-nm spectral range, was used to obtain better wavelength resolution of features identified in the 500-nm scans.

3. IMAGE DIGITIZATION AND PROCESSING

Image analysis techniques were applied to better interpret the cinematic data. This necessitated digitizing the cinematic records. Digitization was accomplished by projecting the photographic images onto a screen and recording the projection to a Super-VHS formatted tape via a professional video camera (JVC, Model HZ-811) and a digital VCR (Panasonic Model AG-1830). The white balance feature of the video camera was used to correct the color bias of the projected image caused by the deviation of the projector lamp from "true white." ("True white" is defined as $I(R)=I(G)=I(B)$, where $I(R)$, $I(G)$, and $I(B)$ are the intensity values of the NTSC "red," "green," and "blue" respectively.) The video tape records were digitized with PC-AT-based frame grabbers to obtain 8-bit monochrome (Truevision, TARGA M8) or 24-bit color (Truevision, ATVISTA) images. A PC-based software package (Jandel Scientific, JAVA) was used for monochrome image analysis. The color image files were ported via a local area network (Ethernet) to a Silicon Graphics Personal Iris 4D20G workstation for analysis. Color image analysis was performed with a UNIX-based software package (G. W. Harraway and Associates, WHIP) which was further developed in-house for the specific needs of this study.

4. TEST MATRIX

This report is based on the results of 33 major tests. A summary of important experimental parameters and the diagnostic techniques employed for each test is given in Table 1. The rationale for choosing various test parameters and diagnostic probes is as follows.

Table 1. Test Matrix of Experimental Parameters and Diagnostic Techniques

Test ^a	Propellant	Inj.Vel. (m/s)	Imaging ^b	Emiss.Spec.	Comments ^{c,e,f}
1	LGP 1845	100	v	--	28 MPa, 480° C, EG&G
2	LGP 1845	100	v	--	seeded w/ Sr(NO ₃) ₂ , 28 MPa, 480° C, EG&G
3	LGP 1845	100-200 ^g	v	--	28 MPa, 480° C, EG&G
4	LGP 1845	110	v	--	480° C, EG&G, 1 mm
5	LGP 1845	100	v	--	480° C, EG&G, 2 mm
6	LGP 1845	110	v	--	38.3 MPa
7	LGP 1845	110	-	250 - 750 nm	
8	LGP 1845	110	v	220 - 345 nm	
9	LGP 1845	110	v	300 - 425 nm	
10	LGP 1845	110	v	425 - 550 nm	seeded w/Sr(NO ₃) ₂
11	LGP 1845	110	v	540 - 660 nm	seeded w/ Ba(NO ₃) ₂
12	LGP 1845	110	v,hsc	660 - 780 nm	seeded w/ LiNO ₃ , 27.6 MPa, HeNe test
13,14	LGP 1845	110	v,hsc	270 - 770 nm	seeded w/ LiNO ₃
15	LGP 1845	110	v,hsc	no signal	seeded w/ LiNO ₃ , cvl
16	LGP 1845	110	v,hsc	270 - 380 nm	seeded w/ LiNO ₃ , cvl
17	LGP 1845	240	v,hsc	--	seeded w/ LiNO ₃ , cvl
18	LGP 1898	110	v,hsc	270 - 380 nm	seeded w/ LiNO ₃ , cvl
19	LGP 1898	110	v,hsc	--	seeded w/ LiNO ₃ , cvl
20	LGP 1898	110	v,hsc	270 - 770 nm	seeded w/ LiNO ₃
21	LGP 1898	240	v,hsc	--	seeded w/ LiNO ₃ , cvl ignition in injector
22	64% HAN ^d	110	v,hsc	no signal	cvl
23	64% HAN ^d	110	v,hsc	no signal	seeded w/ LiNO ₃ , cvl
24	80% TEAN ^d	110	v,hsc	--	seeded w/ LiNO ₃ , cvl
25	H ₂ O	125	hsc	--	cvl, 400° C
26	H ₂ O	95-110 ^g	v,hsc	--	cvl, 530° C, 31 MPa, 1 mm
27	H ₂ O	100-180 ^g	hsc	--	20° C, Tungsten lamp, shadowgraphy, 28 MPa, 3.2 mm
28	LGP 1845	130	v,hsc	--	seeded w/ LiNO ₃ , cvl 34 MPa, 1 mm
29	LGP 1845	150	v,hsc	--	seeded w/ LiNO ₃ + NaNO ₃ cvl, 37 MPa, 1 mm
30,31	Ethanol	150	v,hsc	--	cvl, 480° C, 28 MPa, 1 mm
32	Nitromethane	122	v,hsc	--	cvl, 480° C, 28 MPa
33	Nitromethane/ LGP 1845	141	v,hsc	--	seeded w/ NaNO ₃ , cvl 480° C, 33 MPa

^a Nominal ambient conditions: 500° C, 33 MPa

^b v - video camcorder, hsc - high speed cinematography

^c cvl - copper vapor laser illumination

^d Balance H₂O

^e Unless specified, injection orifice had a 0.5-mm diameter

^f EG&G - xenon strobe

^g Injection velocity accelerated during test.

Of the various Group IA and Group IIA nitrate salts tested for use as flame enhancers, lithium nitrate proved to be the most useful. (This becomes even more evident when image analysis is considered.) The (Group IIA) nitrates of barium and strontium were investigated for use in temperature mapping (Tests #2, #10, and #11). When electronic transitions from the metal atom states of interest were not observed spectroscopically, testing with these salts was discontinued. In Test #12, a 3-mW He-Ne laser beam was passed through the top portion of the windows and its cross-sectional profile recorded photographically. This provided information regarding beam transmission losses and profile broadening due to scattering from liquid droplets, opaque decomposition gases, and index of refraction variations in the chamber. The weight percent of HAN in the solutions injected in Tests #22 and #23 was chosen to be the same as the weight percent of HAN in LGP1845. The weight percent of TEAN in the solution injected in Test #24 was chosen to be the same as the total weight percent of reactive components in LGP1845. Only one experiment involving pure TEAN was conducted because the chamber interior was severely contaminated by tar-like decomposition products created during the test. Experiments with water (Tests #25, #26 and #27) were conducted for general comparison with the propellant sprays and to characterize image degradation due to water vapor condensation. Ethanol and nitromethane tests were conducted to obtain observations of supercritically evaporating sprays (Tests #30, #31, and #32). The nitromethane would not autoignite at the ambient conditions employed. Therefore, an immiscible, 50/50 mixture of nitromethane and LGP1845 was injected (Test #33) to provide an ignition source (combusting LGP1845) for the nitromethane.

5. TEMPERATURE AND PRESSURE PROFILES

A representative sample of chamber pressures and temperatures vs. time for HAN-based propellant tests is shown in Figure 2. The chamber pressure shown is an average from three LGP1845 tests. The chamber temperature shown is also an average of these three tests. Chamber temperature reached its maximum early in the pressurization process and remained stable thereafter. Calibration tests with a 0.125-mm thermocouple established that the response time of the 0.05-mm thermocouple used during the spray tests was less than 5 ms. The temperature in the chamber was determined to be uniform from previous calibration tests in which the temperature at two different locations was measured simultaneously (Birk and Reeves 1988).

Injection took place about 1 second after chamber pressurization. The post-injection temperature traces are distinctly different for each of the four cases. Parameters of interest in these traces are the post-

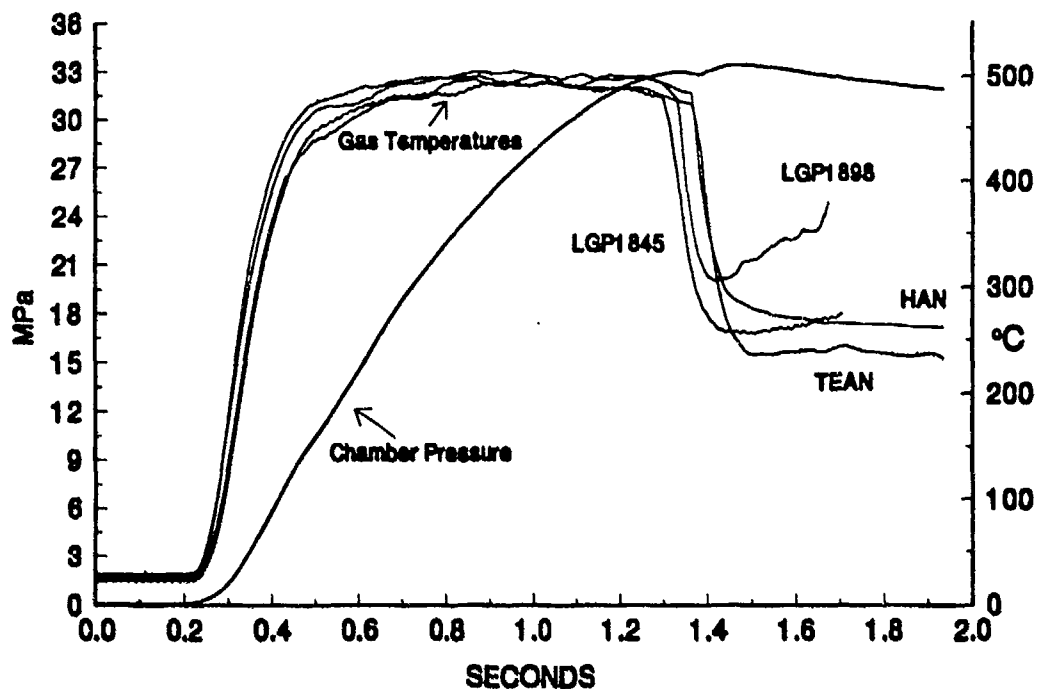


Figure 2. Chamber Pressure and Temperatures vs. Time for HAN-Based Propellants.

injection minimum temperature and the subsequent rate of temperature rise. The minimum temperatures reflect the influence of the propellant's reactivity and its thermal properties. The quality of phase mixing during the early injection period is also reflected in the observed minimum temperatures. The post-injection temperature measured in the HAN test is well above the temperature at which HAN starts to decompose. (This is an important result which is more fully discussed below.) The post-injection temperature measured in the TEAN test is relatively low, indicating that TEAN provided a greater heat sink to the chamber gas than the HAN solutions. The rate of temperature rise is a direct reflection of the reactivity of the given propellant and also provides an indication of flame propagation upstream and inward on the spray. The post injection temperature profiles of the flameless HAN and TEAN sprays are flat. This is consistent with the expectation that both HAN and TEAN, used as monopropellants, release only a small fraction of the energy produced by LGP1845 combustion. The temperature records of the LGP1845 vs. that of the LGP1898 sprays clearly reveal the greater reactivity of the LGP1898 spray.

Figure 3 shows representative chamber pressure vs. time for experiments utilizing 1-mm and 2-mm-diameter orifices. The injection velocities associated with these traces are similar to those generated in tests with the 0.5-mm-diameter orifice; thus, the mass flow rate is proportional to d_o^2 . The sharper pressure drop at injection start for the larger diameter orifices is due to the greater cooling induced by the

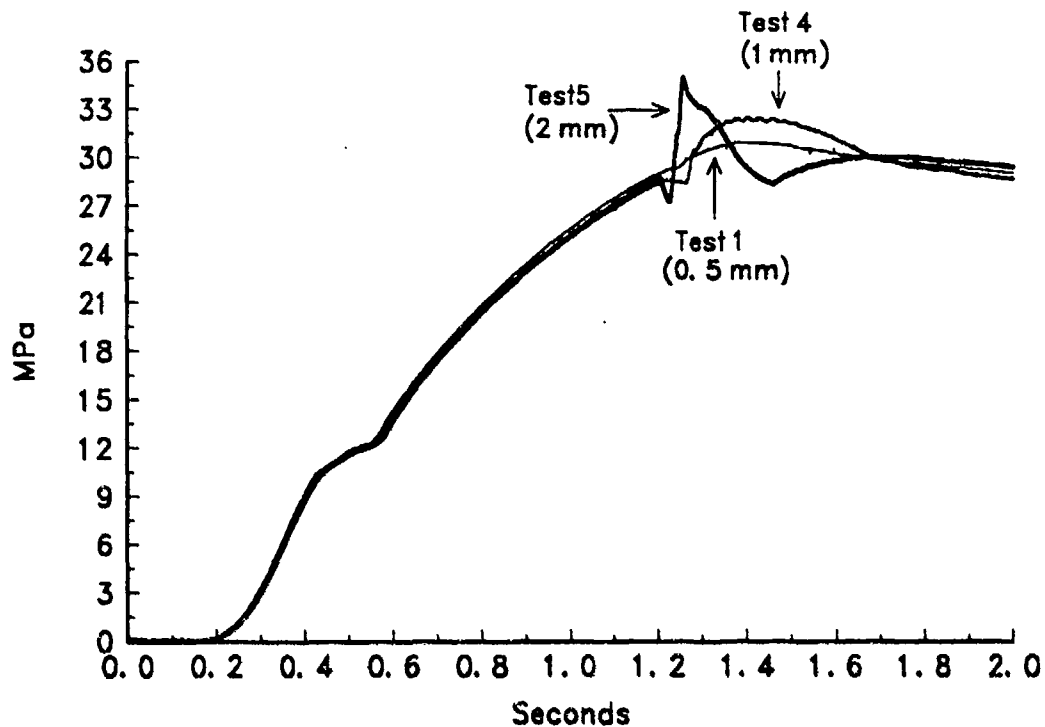


Figure 3. Chamber Pressures for Three Different Jet Sizes.

higher mass flow rate. Once ignited, however, the higher mass flow rates lead to higher pressure excursions. Thermocouple data for the large jets (analogous to that shown in Figure 2) is not presented because it is not considered reliable.

6. SPECTROSCOPIC RESULTS

Emission spectra recorded during an unseeded LGP 1845 test (Test #7) are shown in Figure 4. Only OH A-X emission at 310 nm and Na $3s^2S-3p^2P$ (D-line) emission at 589 nm are identifiable. (Sodium is a propellant contaminant.) These transitions were also observed in LGP1898 tests. Line broadening of the Na D-line is pronounced. The scan-to-scan variation in OH A-X emission intensity is attributable to background level variations. A broad band of emission in the range of 350-550 nm is apparent, but carriers for the signature could not be identified. Emission features were not detected in the HAN or TEAN tests. NO_2 fluorescence, which could have been induced via excitation by the copper vapor laser, was not detected in any test.

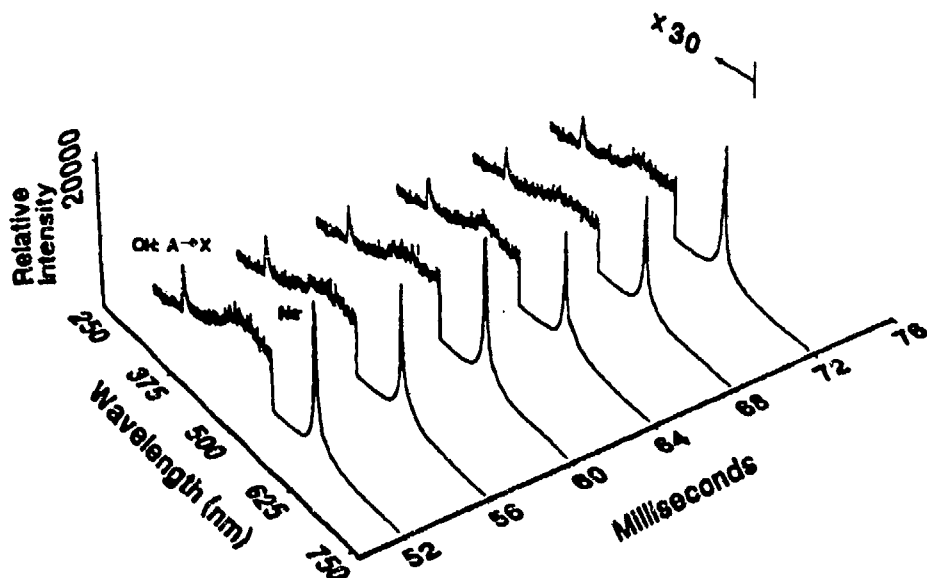


Figure 4. Emission Spectra of Unseeded LGP1845.

In addition to the Na $3s^2S-3p^2P$ transitions observed in all experiments, Li $2s^2S-2p^2P$ transitions were recorded in experiments seeded with LiNO_3 . It was hoped that seeding the propellants with $\text{Sr}(\text{NO}_3)_2$ or $\text{Ba}(\text{NO}_3)_2$ would produce an excited state population distribution of the metal atoms which could be determined from its visible emission spectra. Coupled with color image analysis, this might have permitted mapping of flame temperatures. However, transitions from the Sr and Ba excited states of interest were not observed.

The mechanisms leading to the electronic excitation of lithium and sodium are not known. It seems likely though that a chemiluminescent reaction between M-O ($M = \text{Na}$ or Li) and a combustion intermediate such as N_2O is involved. Such a mechanism would be analogous to reaction of Na-O with various oxidants to produce the mesospheric Na nightglow (Kolb et. al. 1991). Regardless of the excitation mechanism, the energy splitting in the upper state in the Na and Li transitions is insufficient for calculating flame temperature. However, the dominance of these transitions in the emission spectra is useful in image processing, as will be discussed below.

An interesting result of the spectroscopic measurements is the nearly equal intensities of Na^* and Li^* measured in Test #20. (See Figure 5.) In this test, the propellant was seeded with LiNO_3 only, making the number of lithium atoms at least 300 times greater than the number of sodium atoms. Also, the line

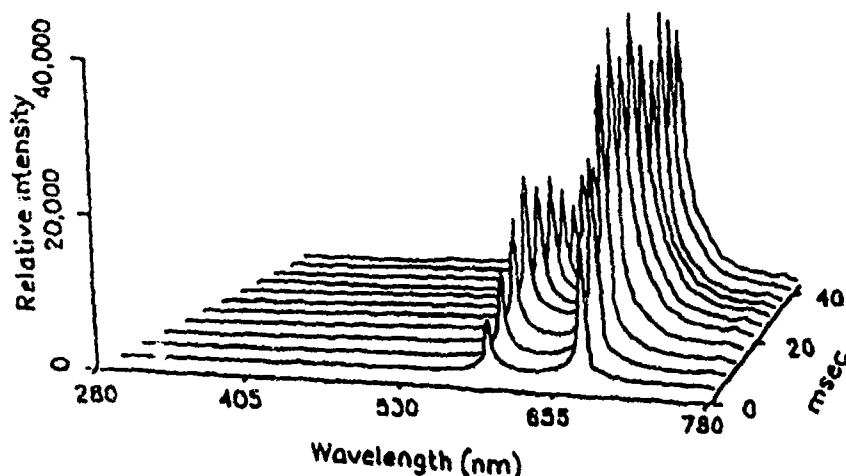


Figure 5. Emission Spectra of LGP1898 Seeded with LiNO₃.

strength of the Li $2s^2S-2p^2P$ transition is slightly stronger than the Na $3s^2S-3p^2P$ transition and lower energy is needed for Li* excitation. Based on these considerations, it was expected that the intensity of the Li* transition would be much greater than the Na* transition. One possible explanation for this result is that the decomposition temperature of NaNO₃ (280° C) is significantly lower than that of LiNO₃ (600° C). This possibility and its potential for temperature mapping will be more fully explored in the future.

7. PHOTOGRAPHIC OBSERVATIONS AND ANALYSIS

7.1 GENERAL OBSERVATIONS

The video and the high-speed cinematography provide visual records with distinctly different time scales and exposure requirements. The video pictures are a collection of 1-ms exposure "snapshots" every 1/60 of a second. As such they do not detail the dynamics of the sprays. However, the relatively low exposure requirements of the video CCD element facilitate the capture of "global" features created by sidelighting the spray with an EG&G xenon strobe light. (This strobe is not sufficiently intense for use in sidelit high-speed cinematography.) Because a video frame corresponds to the integration of spray variations over 1 ms, the penetration distances and divergence angles of the sprays are well defined. (See Figures 6, 7, and 8.) The unreacted portion of the spray appears distinctly blue corresponding to the rich blue wavelength content of radiation from the xenon lamp. Conical spray outlines which have vertices corresponding to the injection port are observed in the video pictures. This is clear evidence that

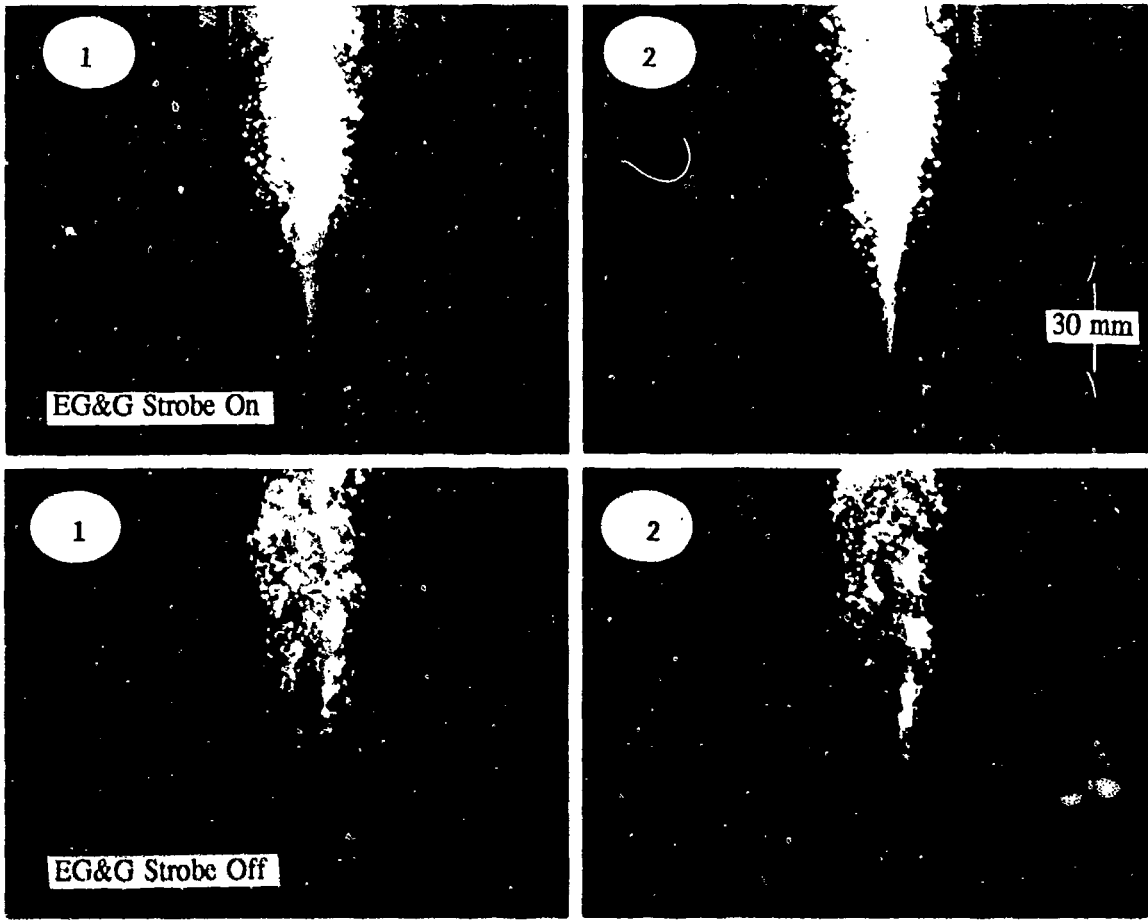


Figure 6. Video Pictures of 0.5-mm LGP1845 Jet (Test No. 1).

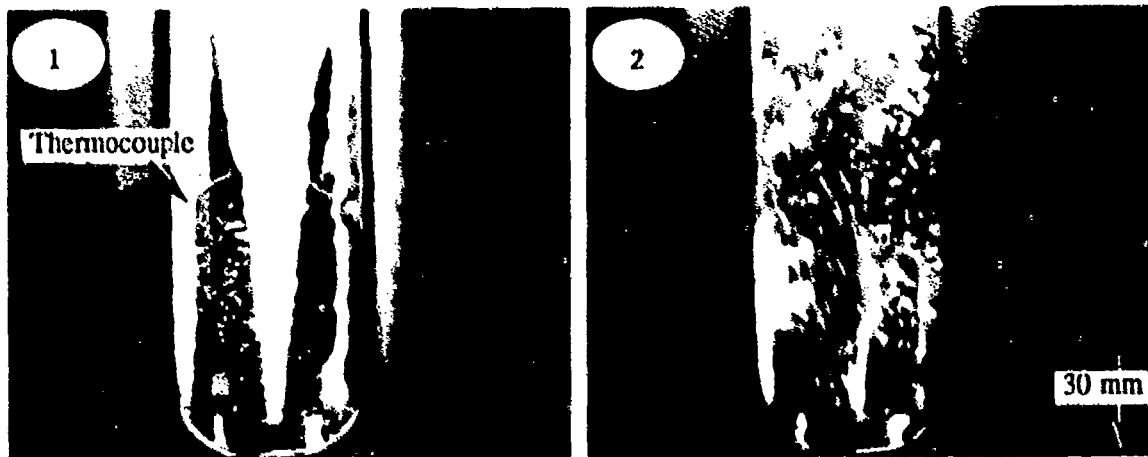


Figure 7. Video Pictures of 2.0-mm LGP1845 Jet (Test No. 5).

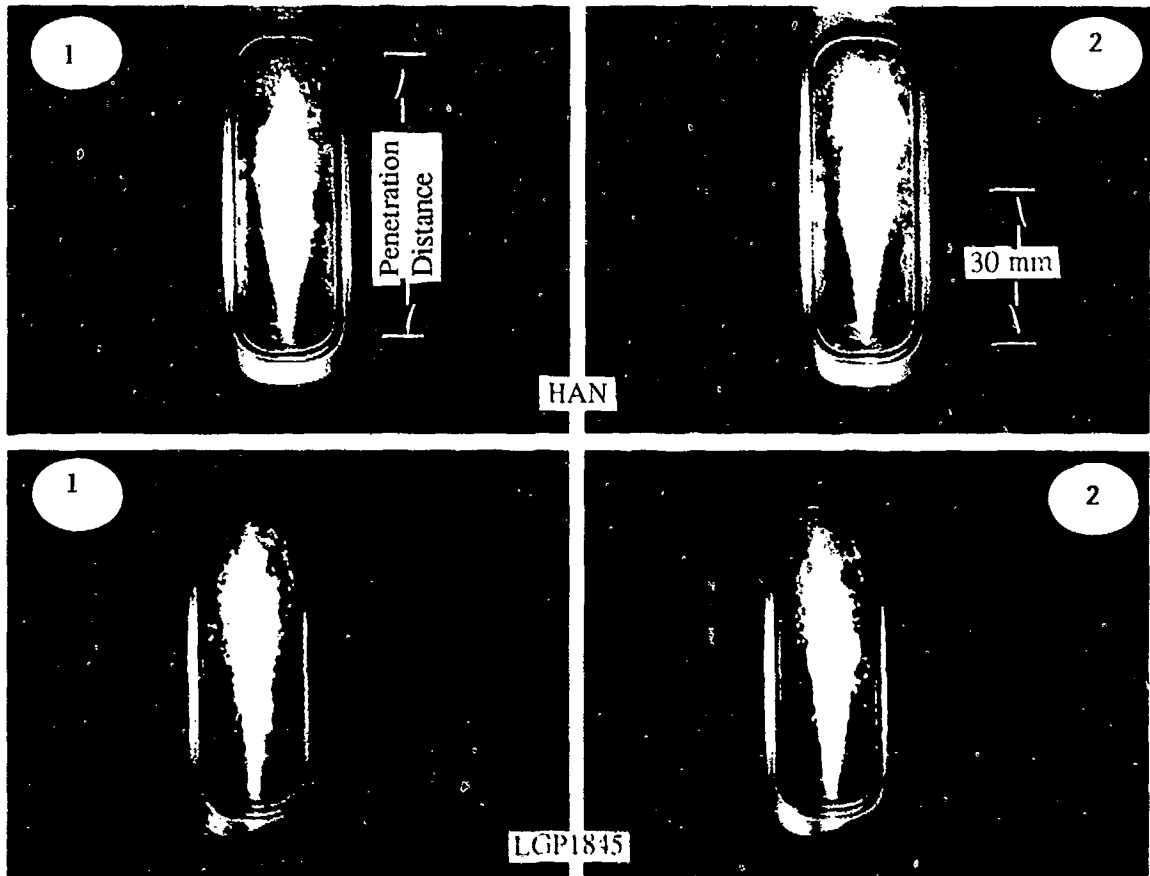


Figure 8. Video Pictures of 0.5-mm Jets of HAN and LPG1845 (Test Nos. 23 and 15).

all tests were within the atomization regime. Flame is observable in these images by its bright orange to red color.

The cinematic records reveal the actual spray dynamics occurring in these experiments. Sidelighting with the copper vapor laser strobe and seeding the propellants with nitrate salts provided breakthroughs in high speed imaging of the sprays. Sidelit photography produced more informative images than (the commonly used) backlit photography. Imaging of scattered light is less sensitive to the index of refraction variations prevalent in high pressure gas than imaging shadows produced by backlighting. Liquid boundaries appear clearly against the black background when sidelighting was used. Seeding the propellants with nitrate salts created sufficient additional combustion luminosity for flame to be recorded at the high framing rates necessary to capture the spray dynamics.

The cinematic records reveal an increase in turbulence as the injection proceeded. Flame spreading upstream on the spray is commensurate with the increase in turbulence. In all combusting sprays burning was most intense in vortices adjacent to the spray envelopes. The slow accumulation of opaque gases in the chamber indicates that LPG1845 did not burn with optimum efficiency. The He-Ne test (#12) shown

in Figure 9 demonstrated that the index of refraction variation due to thermal fluctuations in the dense ambient gas, though present, did not significantly distort light transmission. Based on this test, we estimate that submillimeter size particles can be measured from the cinematic records with reasonable accuracy. Indeed, surprisingly large drops on the order of 1 mm in diameter are observed in the records. This result indicates that coalescence of droplets was a significant process in these tests.

Another observation from Test #29 was that, when passed through the spray near its tip, the He-Ne beam diffused due to diffraction from the drops. Based on this result, future consideration will be given to image analysis of laser beam diffraction patterns recorded on the high-speed film. A commercially available instrument (Malvern) measures particle size distribution in sprays by passing a laser beam through the spray and detecting diffraction patterns projected by a lens onto a solid-state ring detector. The use of film in lieu of a ring detector would allow compensation for beam steering. In addition, the use of a multiple line laser, creating a corresponding number of diffraction patterns which could be separated via color image analysis, could provide more accurate particle sizing than obtainable using a monochromatic source.

7.2 COMPARATIVE SPRAY DYNAMICS

7.2.1 COMBUSTION INTENSITY vs. ORIFICE DIAMETER

Figures 6 and 7 represent the two extremes of orifice diameters utilized in the combustion experiments. These tests correspond to injections through 0.5-mm and 2.0-mm-diameter orifices, respectively. The flame anchored about 20 mm from the injector nozzle in the test with the 0.5-mm-diameter orifice. Quasisteady combustion, defined as the time when flame reached this distance from the nozzle, lasted up to 0.3 seconds in the injections through the 0.5-mm orifice. Large (ca. 1 mm) liquid particles were observed burning about the spray envelope. Despite the rather long exposure time (1 msec), the particle boundaries appear distinctly sharp, indicating very low local velocities. In contrast, the streaking associated with particle trajectories in Figure 7 indicate high local velocities and turbulence in the test with the 2.0-mm-diameter orifice. This is due to the higher mass flow rate. Combustion lasted for less than 50 ms (two to three video frames) in this test. The thermocouple in the middle of the chamber is discernibly bent, indicating that the intact liquid core is impinging on it.

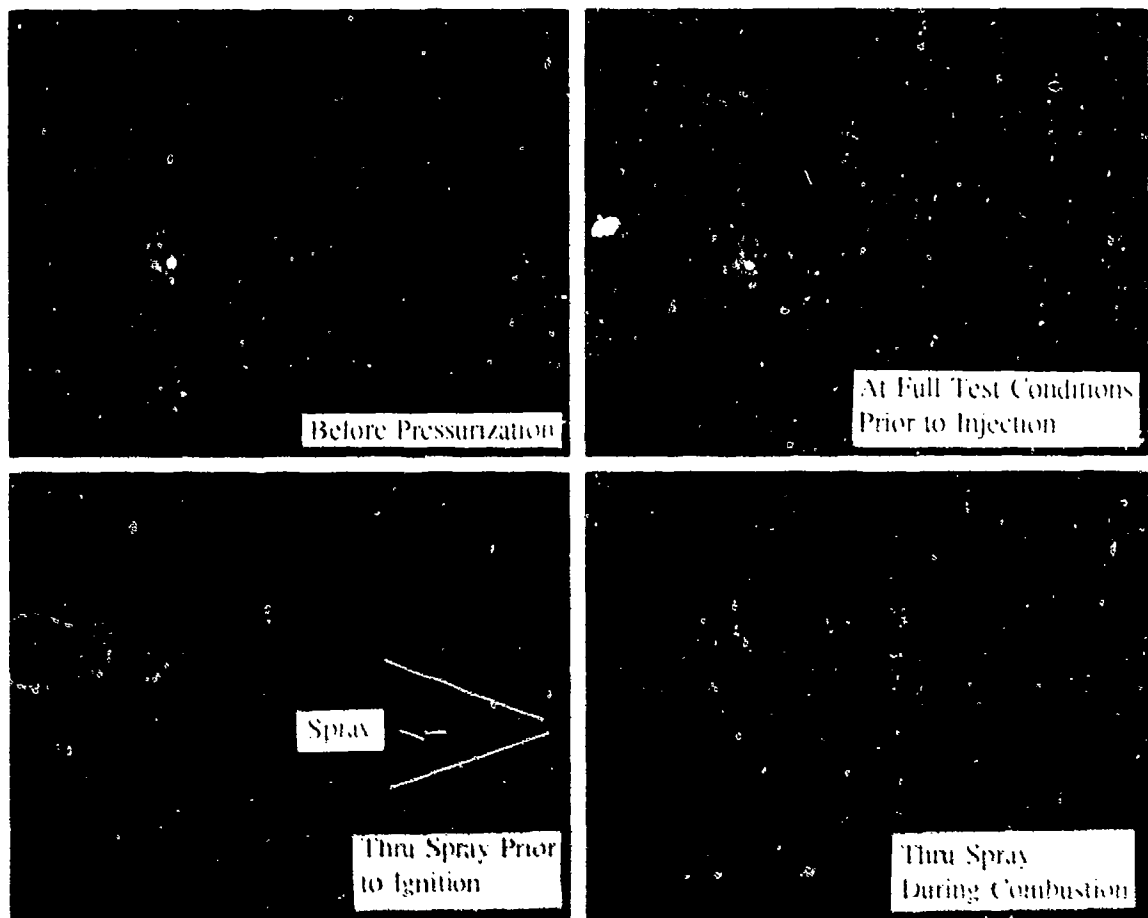


Figure 9. Cine Pictures of HeNe Beam Through Test Section (Test No. 12).

7.2.2 HAN VS. LGP1845 SPRAY DYNAMICS

Figure 8 compares HAN and LGP1845 sprays generated with similar experimental parameters. Of interest is the distance from the injector to the point where the spray is totally converted to gaseous products. (This is defined as the penetration distance.) The similarity of the penetration distances measured for these two sprays supports the assertion that the HAN decomposition is the rate limiting step in LGP1845 spray combustion (Carleton, 1990). The yellow coloration of the tip of the HAN spray is probably due to the 578.2 nm line of the copper vapor laser. The 510.6 nm line may be absorbed preferentially by NO_2 , a HAN decomposition product.

7.2.3 HAN VS. TEAN SPRAY DYNAMICS

The dynamics of the HAN and TEAN sprays, shown in Figures 10 and 11, are much alike. The similar penetration distances observed for these two sprays indicates that the time scale for TEAN decomposition is the same as that of the HAN under the given test conditions. Obscuration of the spray details due to opaque decomposition products proceeded somewhat faster in the TEAN experiment. In

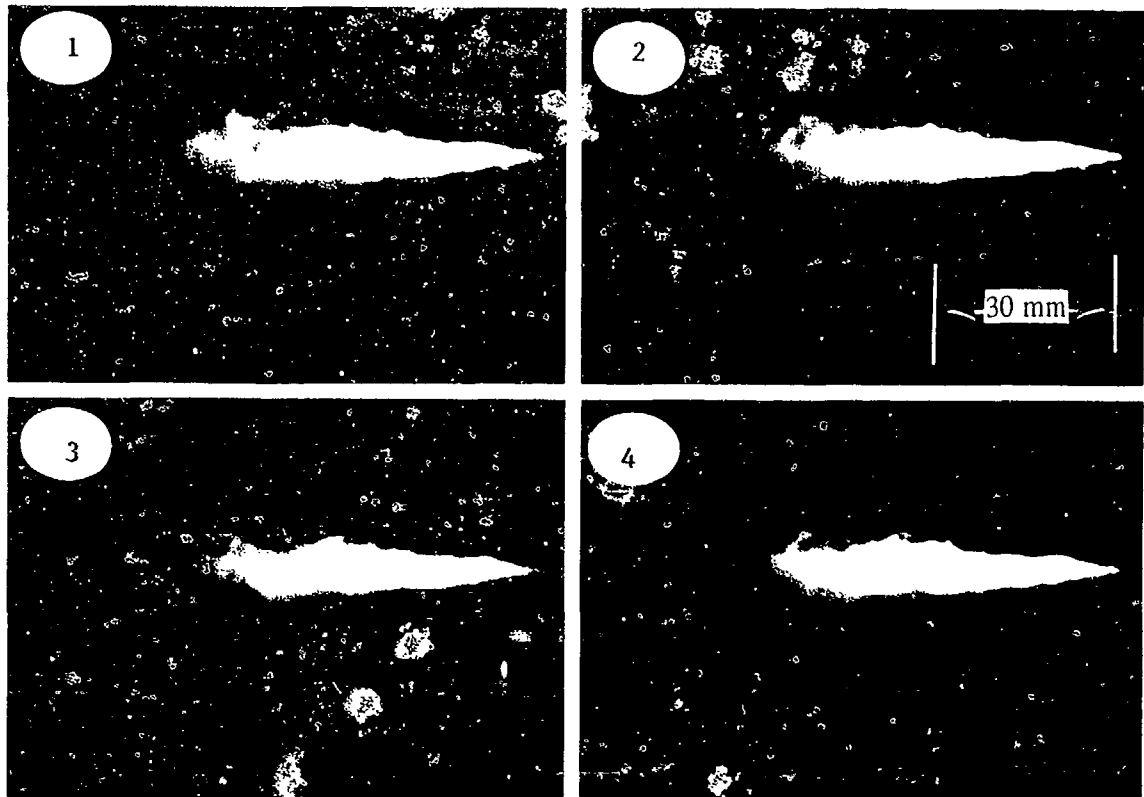


Figure 10. Cinematic Sequence of HAN Spray (2,000 frames/s, Test No. 23).

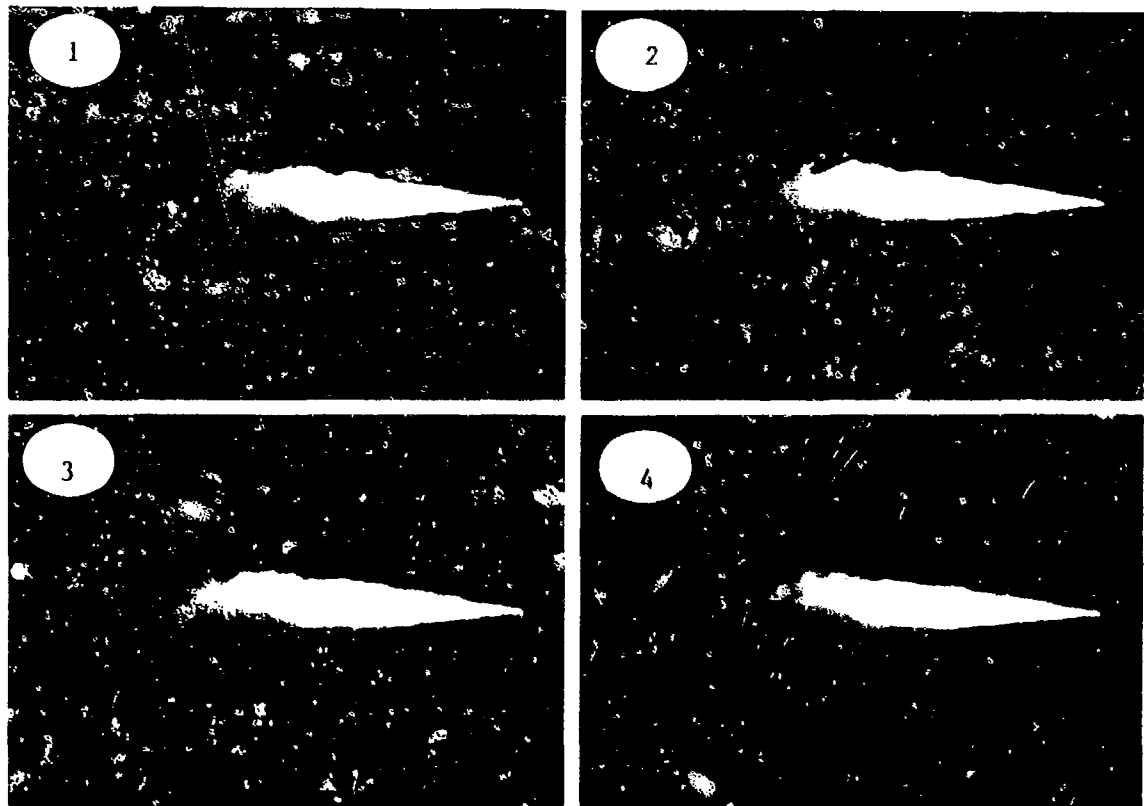


Figure 11. Cinematic Sequence of TEAN Spray (2,000 frames/s, Test No. 24).

both sprays, large particles are observed around the tip vortex region. The color of the HAN spray is more yellow than that of the TEAN spray which is presumably due to the fact that they have different decomposition products. Emission of visible light due to decomposition or combustion was not observed in either spray. The lack of visible emission is consistent with the low reactivity and heat generation in these sprays indicated previously via the thermocouple measurements.

7.2.4 LGP1845 VS. LGP1898 SPRAY DYNAMICS

Figures 12 and 13 compare the sidelit spray combustion of LGP1845 and LGP1898 under similar experimental conditions. Figure 14 shows a comparison of these sprays in the absence of external lighting. The newly formulated LGP1898 (Klein et al. 1991) clearly exhibited more reactivity than LGP1845. One manifestation of the increased reactivity is the extent to which the LGP1898 spray bulges compared to the LGP1845 spray. Also, LGP1898 burned to completion while LGP1845 did not. Flame advanced within 15 mm of the injector in the case of LGP1898. Large, burning liquid particles and burning in vortices are evident in both cases.

To quantitatively establish the intensity, extent, and temporal characteristics of combustion, intensity histograms of consecutive (monochrome) images produced in the absence of external illumination (Tests #13 and #20) were constructed. Intensity histograms of the flames depicted in Figure 14 are shown in Figures 15 and 16. The gray levels in the histograms correlate with flame intensity and have a dynamic range from 0 (total darkness) to 255 (CCD element saturation). The number of pixels per gray level range is proportional to the projected area of the corresponding luminosity level. Such histograms provide the potential to correlate "combustion noise" with pressure fluctuations. For the high luminosity values (gray levels above 200) the histograms for the LGP1845 and the LGP1898 flames are comparable. Since the high luminosity values are (presumably) associated with the large, burning droplets, the histograms indicate that the dynamics of the LGP1898 and LGP1845 sprays are similar with respect to droplet formation and burning.

7.2.5 WATER SPRAYS

Cinematic images of water injected through a 1-mm-diameter orifice are shown in Figure 17. The images indicate extensive evaporation, and a penetration distance which (apparently) did not extend much beyond the window length (97 mm). The critical point of water is 374° C and 22.1 MPa. Although the

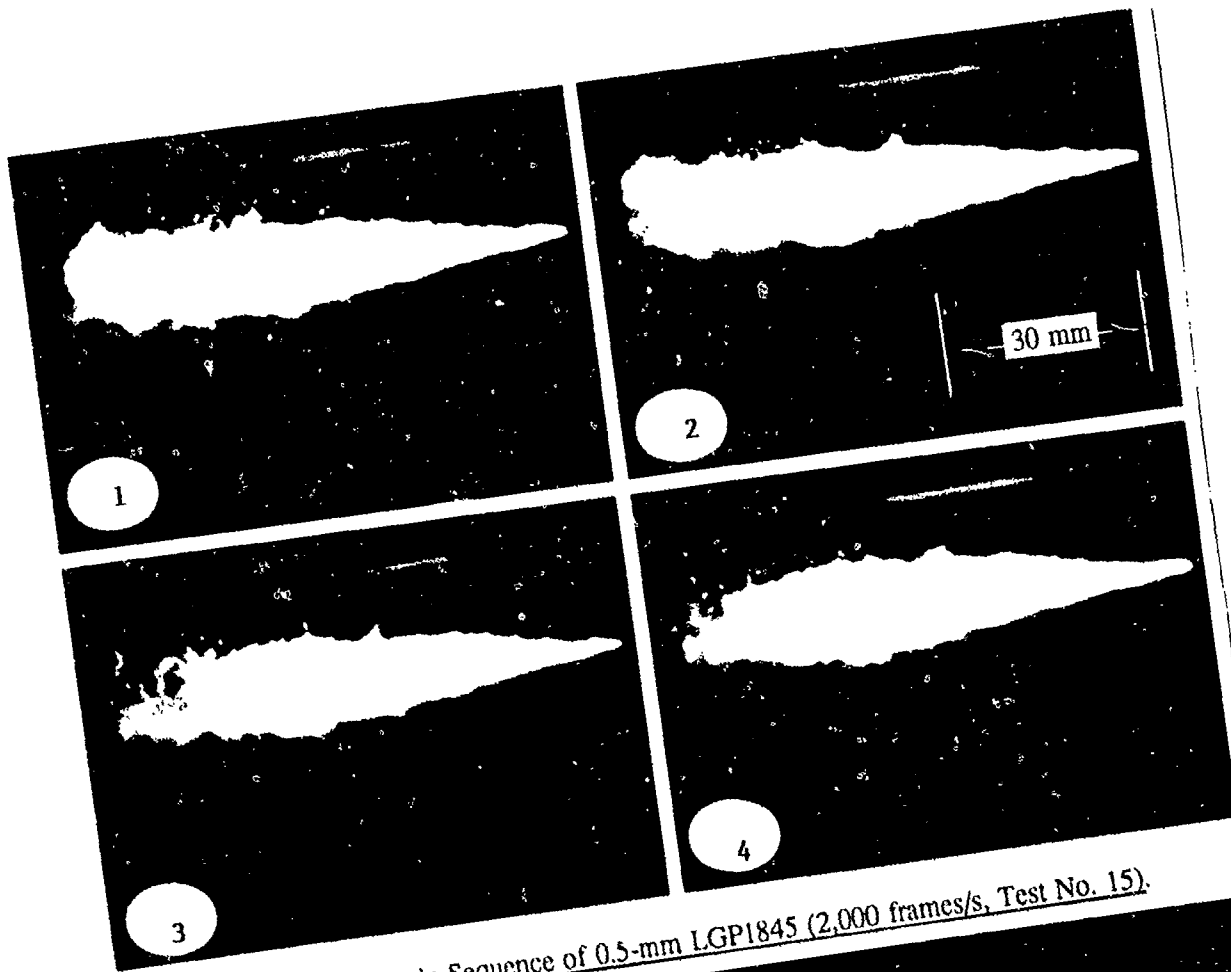


Figure 12. Cinematic Sequence of 0.5-mm LGP1845 (2,000 frames/s, Test No. 15).

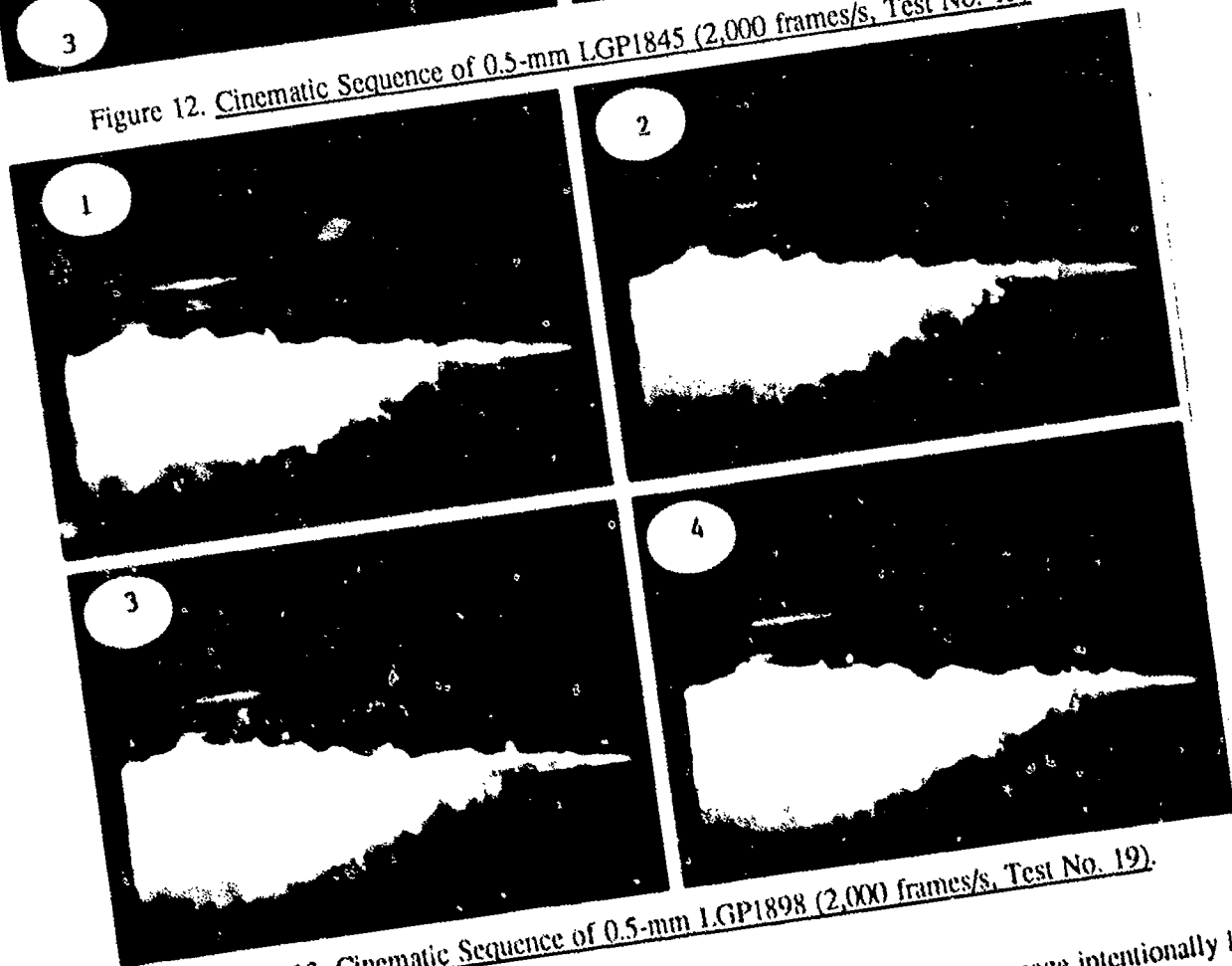


Figure 13. Cinematic Sequence of 0.5-mm LGP1898 (2,000 frames/s, Test No. 19).

Following page intentionally left blank.

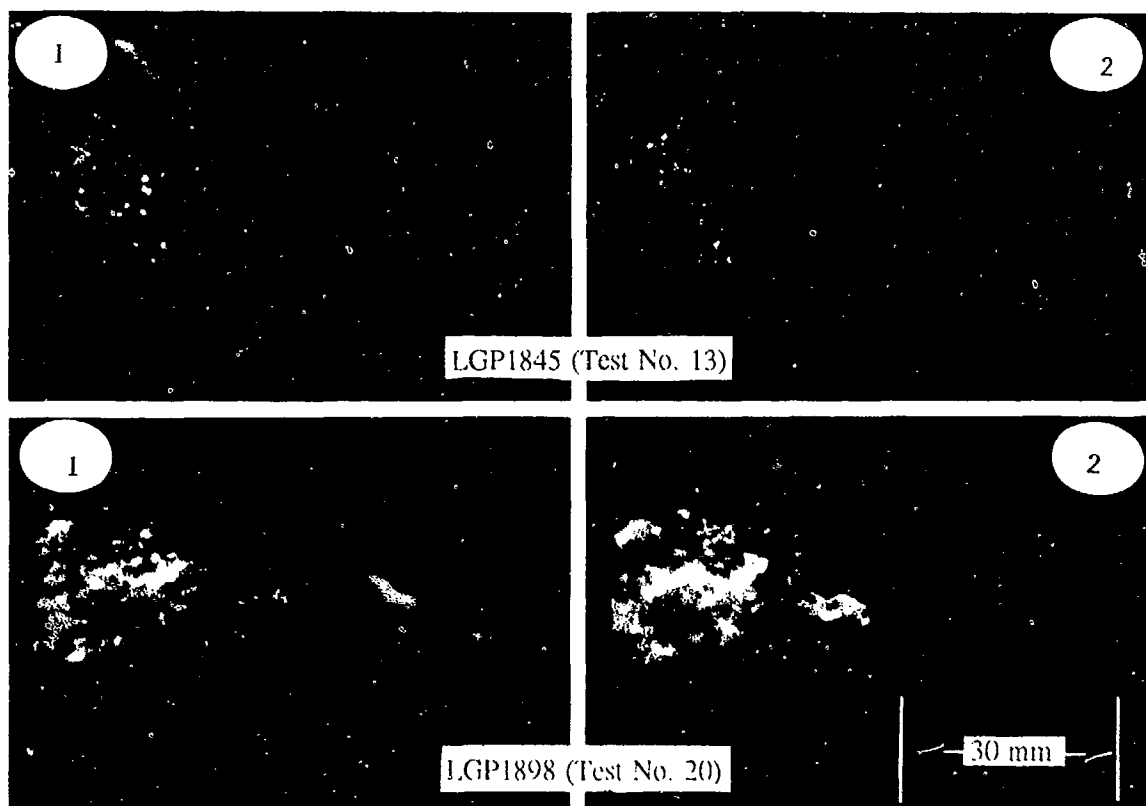


Figure 14. Cinematic Sequences of Flames of 0.5-mm LGP1845 and LGP1898 (2,000 frames/s, Test Nos. 13 and 20).

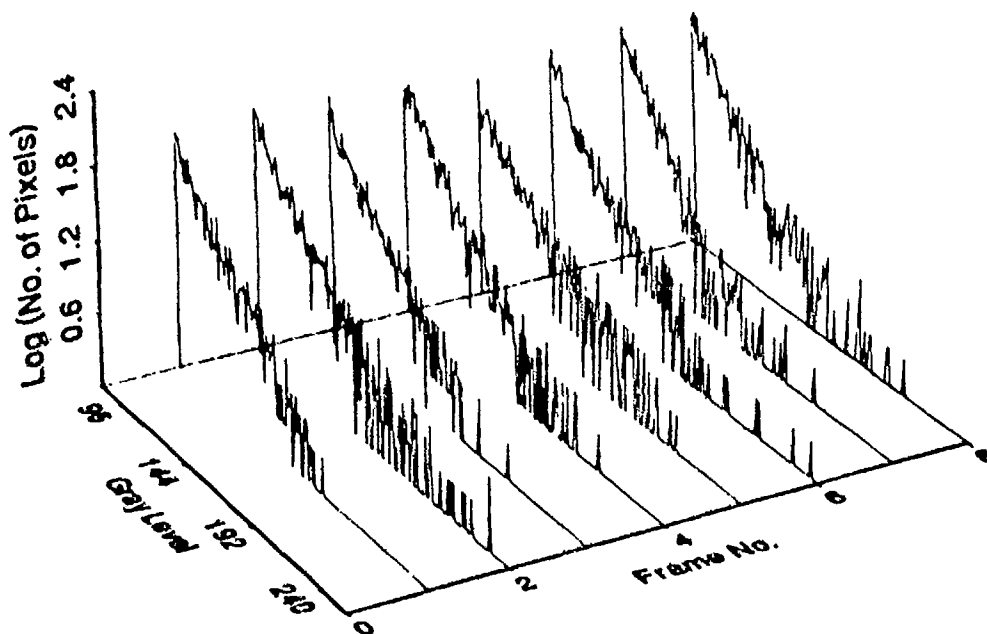


Figure 15. Intensity Histogram of LGP1845 Flame (Test No. 13).

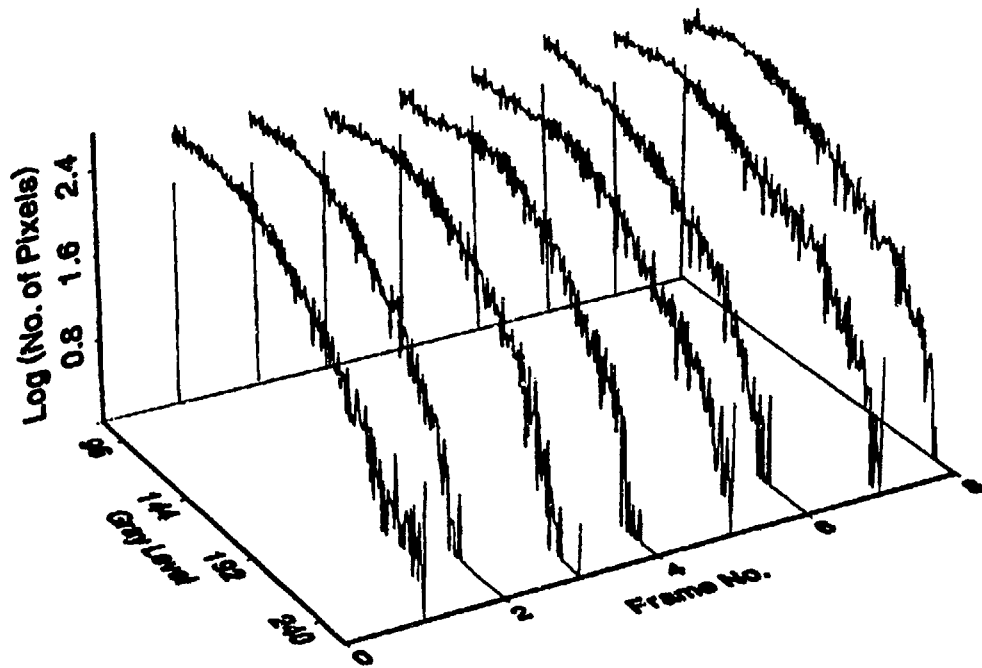


Figure 16. Intensity Histogram of LGP1898 Flame (Test No. 20).

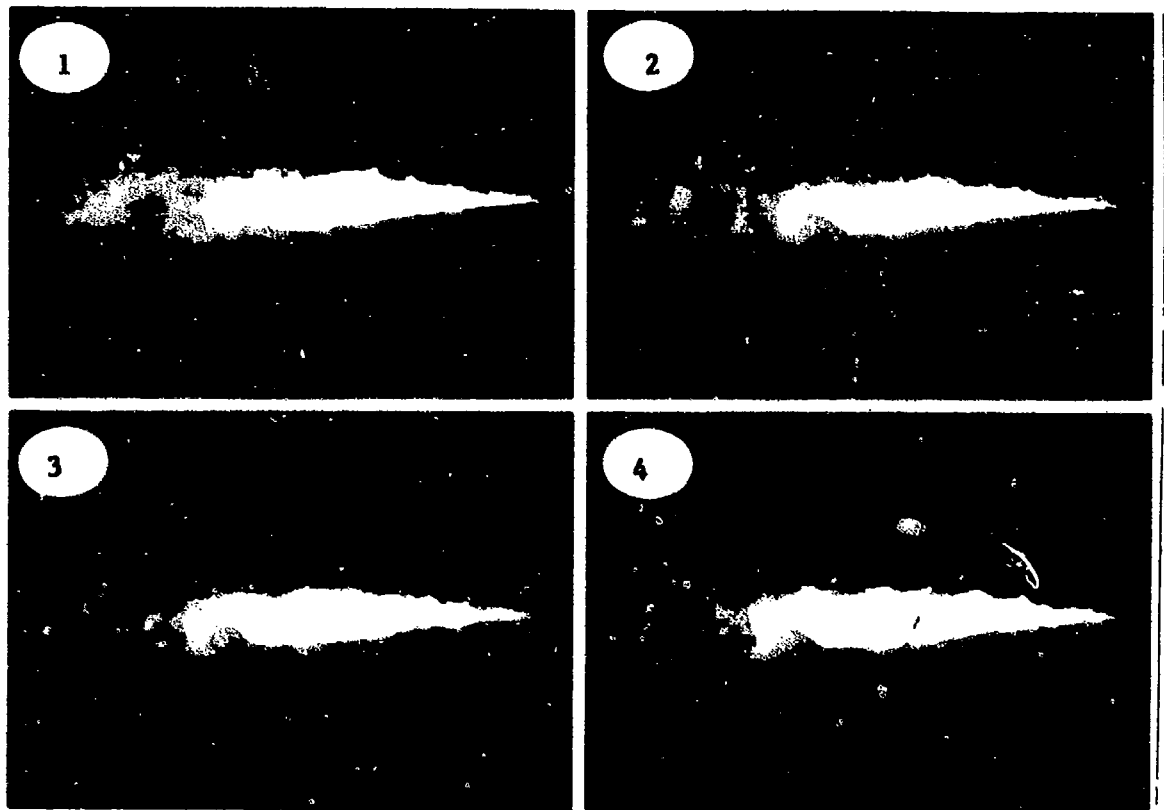


Figure 17. Cinematic Sequence of 1-mm Evaporating Water Sprays (5,000 frames/s, Test No. 26).

ambient temperature and pressure are (moderately) above these values, the formation of large water drops was not precluded. Water is a major constituent of the HAN-based propellants and is expected to control the atomization characteristics and heating rates of the spray particles in some measure. Since the critical points of the water-solvated propellants are higher than water, it was expected and indeed observed that these propellant sprays exhibited behavior characteristic of subcritical combustion. That is, combustion progress in the LGP tests depended to a large degree on liquid particle trajectories.

7.2.6 SUPERCRITICALLY EVAPORATING SPRAYS

Figures 18 and 19 show selected sequences from experiments with nitromethane and ethanol. The critical points of nitromethane and ethanol are 315° C, 6.3 MPa, and 243° C, 6.4 MPa, respectively (Handbook of Physics and Chemistry 1986). These are well below the ambient gas conditions. No large particles could be discerned in the cinematic records of either of these sprays. Both sprays exhibited intermittent segmentation of their structure as well as corkscrewing and rapid deviations of the spray axis about the nominal centerline. These dynamics are much different than those of the subcritical sprays. Also, the divergence angles and penetration distances of sprays into supercritical ambient conditions are smaller than those of sprays into subcritical conditions. The nitromethane, though a monopropellant, did not ignite. The penetration distance for nitromethane injected through a 0.5-mm orifice was found to be half that of ethanol injected through a 1.0-mm orifice. (See Section 9.4.)

7.2.7 SPRAY COMBUSTION OF LGP1845/NITROMETHANE SPRAYS

Figure 20 shows the injection of a 50/50 LGP1845/nitromethane mixture through a 0.5-mm-diameter orifice (Test #33). Although not miscible, some "mixing" occurred during injection which established concentration gradients of the propellants. The injected mixture started as pure LGP1845 and became progressively richer in nitromethane. Unlike the injection of pure LGP1845 through a 0.5-mm-diameter orifice, this mixture burned to completion. The nitromethane, which did not autoignite (Test #32), was presumably ignited by burning LGP1845 particles. Since the LGP1845 and the nitromethane are immiscible, this spray was expected to exhibit a combination of both supercritical and subcritical dynamics. If this was indeed the case, the large particles observed in Figure 20 are the LGP1845 component. Because the flame temperature of the nitromethane is about 1,000° C higher than that of the LGP1845, it is possible that the local ambient gas temperature around the LGP1845 particles was much higher than in pure LGP1845 spray experiments. Nevertheless, the formation of large LGP1845 particles

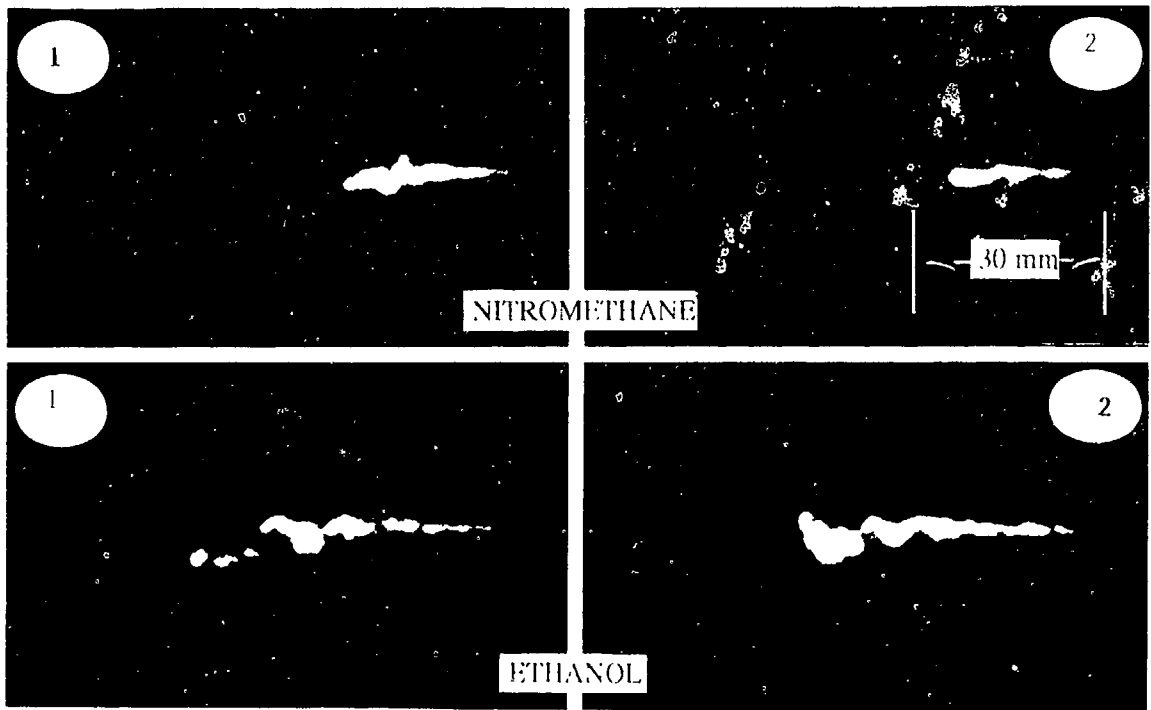


Figure 18. Supercritical Evaporation, 0.5-mm Nitromethane (Test No. 32) and 1-mm Ethanol (Test No. 34)
(Sequences at 5,000 frames/s).

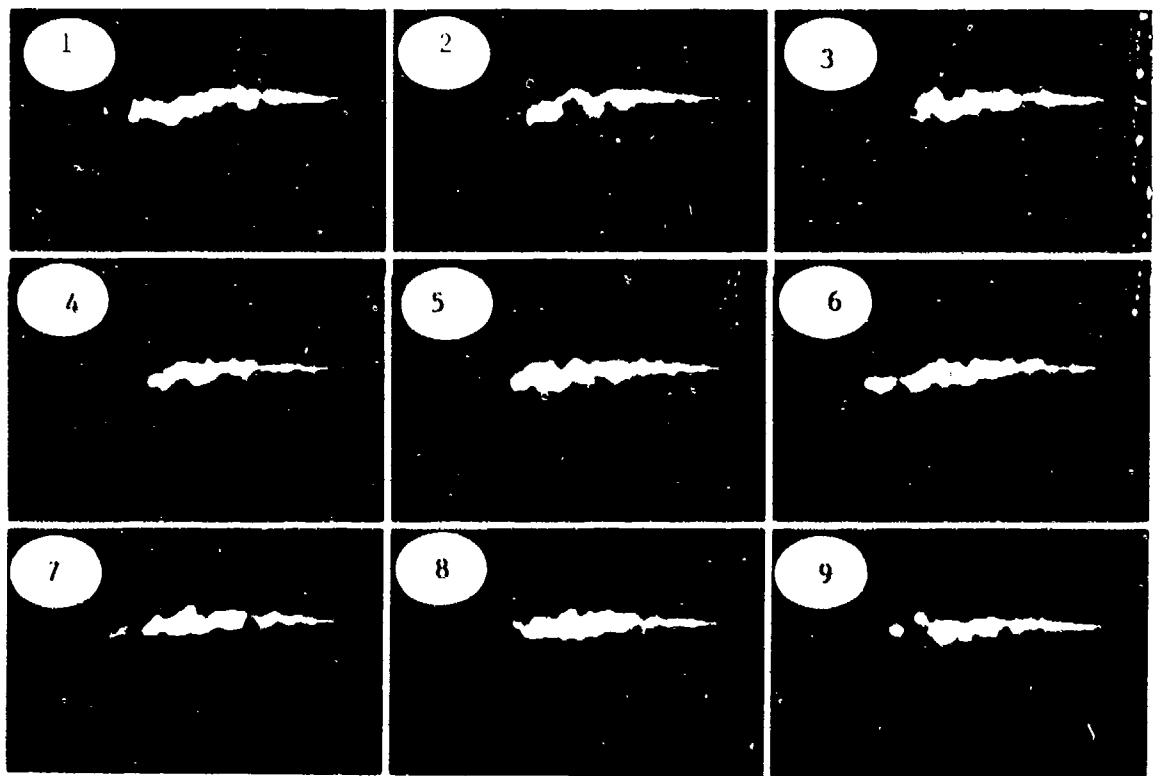


Figure 19. An 1.8-ms Sequence of Supercritically Evaporating 1-mm Ethanol Jet Demonstrating High
Degree of Structural Fluctuation (Test No. 31).

is observed in these figures. An interesting aspect of this spray is the intermittent shedding of large segments of the spray from its tip. (This is similar to the pure supercritical evaporation depicted in Figures 18 and 19.) The segments then burn in a large vortex beyond the spray tip. This behavior is distinctly different than that of pure LGP sprays.

7.2.8 HIGH INJECTION VELOCITY SPRAYS

In tests #17 and #21, the propellants were injected at 240 m/s (Figure 21). (Although termed "high velocity," 240 m/s is less than 20% of the injection velocities typical in guns.) The LGP1845 decomposed completely within the field of view, but burning was less complete than in the lower velocity injection tests. Commensurate with the high velocities, more frequent shedding of vortices from the boundaries is observed. The high-velocity test with the LGP1898 was catastrophic. About 10 ms after the onset of injection, the injector top sheared away due to the ignition of the propellant inside the injector. Prior to the explosion, the jet emerging from the injection orifice thickened significantly. This observation may indicate that viscous heating ignited the propellant inside the injector. Viscous heating has been suspected in the ignition of LGP1845 in small orifices at injection velocities above 240 m/s (Messina et al. 1990). However, these earlier findings involved flows in which cavitation was likely. Cavitation should not have occurred in the present tests due to the design of the injector. Its regenerative principle of operation results in low cavitation numbers. The sensitivity of LGP1898 to viscous heating is unknown.

8. COLOR IMAGE PROCESSING AND ANALYSIS

Color image processing was useful for enhancing the details of images involving laser illumination. As discussed earlier, the spectroscopic data show that the flame of combusting lithium nitrate-doped LGPs 1845 and 1898 can be considered to have just two wavelength components, the 589.0-nm emission line of sodium and the 670.7-nm emission line of lithium. The copper vapor laser radiates at 510.6 nm and 578.2 nm. Thus, the color images effectively result from the combination of just four different wavelengths. The relative amounts of I(R), I(G), and I(B) produced for unit exposure of the high-speed film (Kodak, Ektachrome 2253) at these four wavelengths were approximated from the published spectral sensitivity curves. The relative amounts determined in this manner are shown in Table 2. This table shows that the 510.6-nm laser line is the only color source which contributes to I(B). Likewise, I(R) is

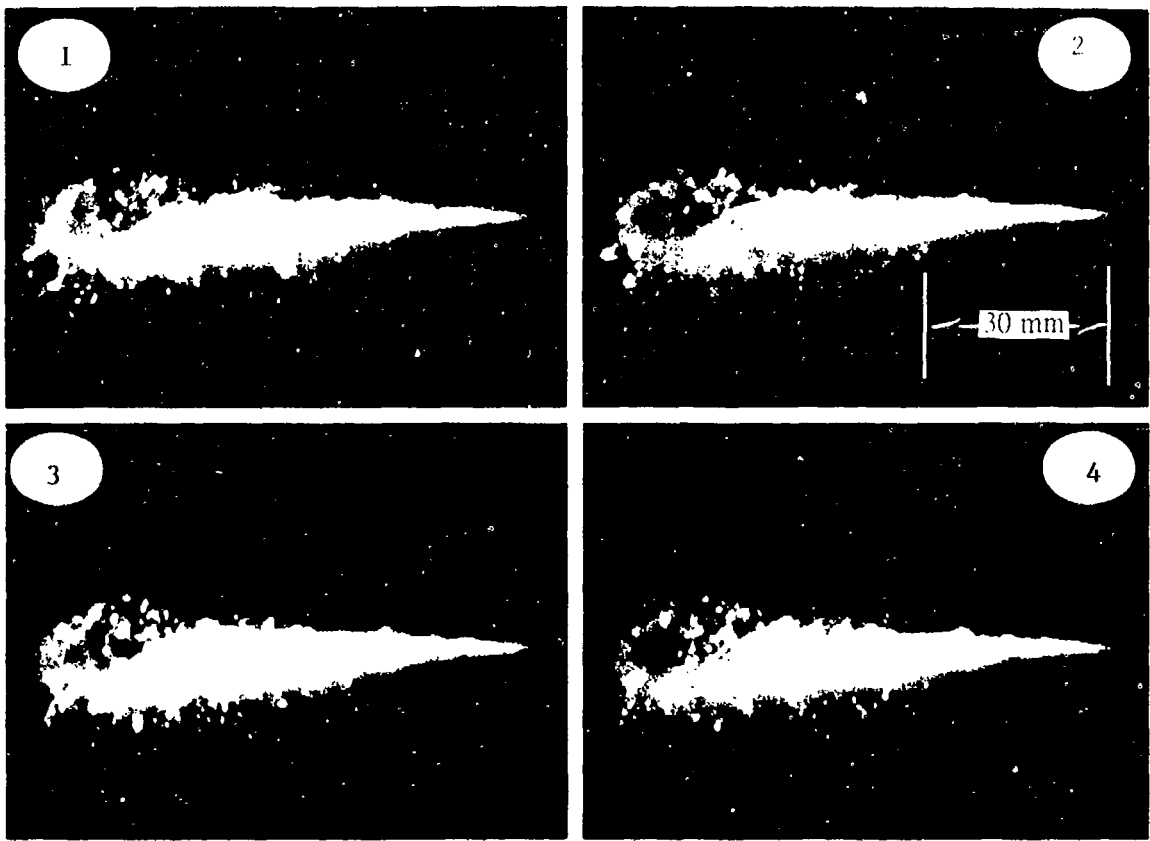


Figure 20. Cinematic Sequence of 0.5-mm LGP1845/Nitromethane Jet (5,000 frames/s, Test No. 33).

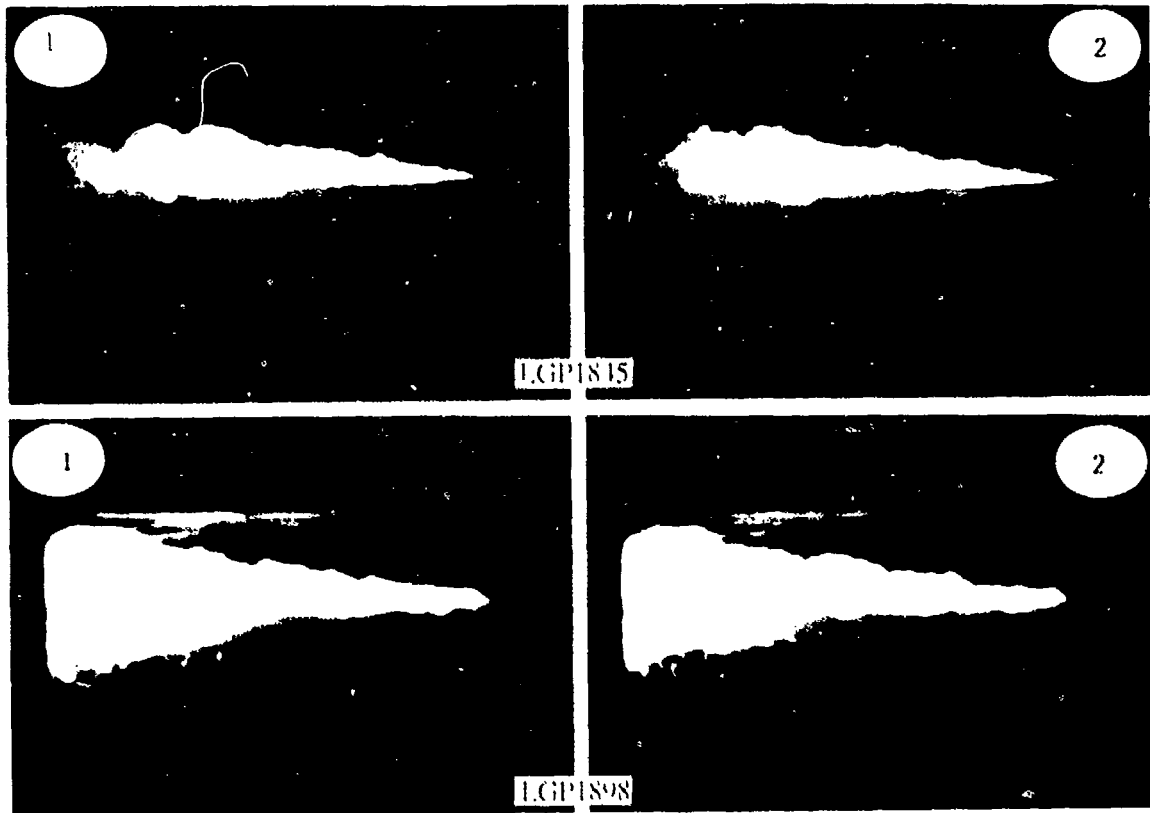
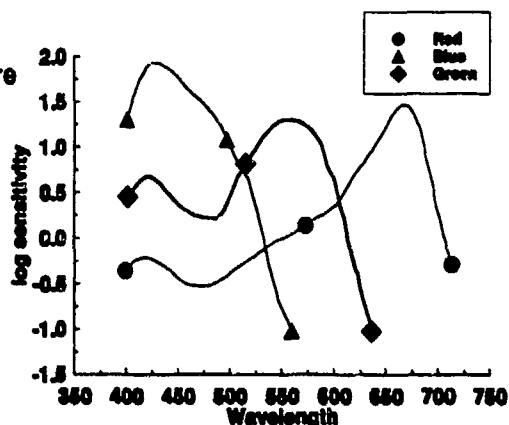


Figure 21. High Injection Velocity Tests with 0.5-mm Jets of LGP1845 and LGP1898 (Tests Nos. 17 and 21).

Table 2. Film Response to Prevalent Wavelengths in Burning Spray Illuminated by Copper Vapor Laser

RGB Sensitivity v. Selected Wavelengths for Unit Exposure
(Kodak Ektachrome 2253 High Speed Daylight Film)

Wavelength (nm)	R	G	B
510.6	0.5	6.1	5.9
578.2	1.6	15.1	<0.1
589.0	1.8	8.4	<0.1
670.7	27.5	<0.1	<0.1



predominantly due to emission from lithium. Thus the color content of the images provides a means of identifying contributions due from flame and laser scatter from liquid in regions where these two processes are coincident.

It should be noted that the film color sensitivity data has only been established for exposure times ranging from 10^0 to 10^{-4} seconds. Exposure durations outside this range necessitate corrections for color biasing and/or f-stop. Since the film's exposure to flame is controlled by the framing rate of the camera ($<10^4$ fps), the published data should provide reasonable values for color analysis of flame. The film's exposure to laser scatter, however, is determined by the duration of the laser pulses which are 2.5×10^{-8} seconds long.

To establish sensitivity data for the 2.5×10^{-8} -second exposure to laser scatter, images from experiments involving the injection of H_2O were analyzed. For these experiments, the image is solely a product of laser scatter. We found that the I(B):I(G) ratio in these images is close to 1:1.2 vs. the 1:2 ratio calculated from the values in Table 2. This deviation may be due to light scattering phenomena. The effective cross section for light scattering from particles changes with their size and index of refraction in accordance with the Mie theory. For particles of submicron size (Rayleigh), scattering efficiency is greater at shorter wavelengths. Hence, for finely atomized sprays undergoing significant evaporation, it is possible that the 510.6-nm laser line scattered more effectively than the 578.2-nm line. This would result in an image with higher than expected blue content.

While this explanation may account for the observed ratio deviation, other factors (such as variations in the developing process) are probably also important. And combusting sprays have additional considerations. For example, the known LGP1845 combustion intermediate NO_2 has an absorption cross section which is much higher at 510.6 nm than at 578.2 nm. Preferential absorption of the 510.6-nm line would tend to lower the I(B):I(G) ratio. Since it was not possible to quantitatively assess all the factors which could have affected the color balance, we focused on noise reduction and image enhancement based on the simple process identification criteria noted above. That is, I(B) is associated with laser scatter and I(R) is associated with flame emission.

Criteria to identify noise in the images was established by sampling background regions which should have been black (I(R)=I(G)=I(B)=0). I(G) values were particularly instructive in this regard because both emission from the combustion process and laser scatter produce images with I(G) values. (See Table 2.) From this analysis, a threshold characteristic of true signal was determined.

The next aspect of the analysis involved enhancing the details of gas-liquid interaction. This was approached by calculating the I(R):I(B) ratio on a pixel by pixel basis. A large I(R):I(B) ratio indicates a high contribution due to emission from flame while a low ratio indicates a high contribution due to laser scatter from liquid particles. (Because both flame emission and laser scatter produce images with I(G) values, I(G) values do not provide information which delineates the combustion process from the laser scatter.) The pixels were then mapped to a pseudocolor based on the I(R):I(B) ratio. Additionally, the intensity of each pseudocolor pixel was modulated in proportion to its total intensity (I(R)+I(G)+I(B)) in the original image. Intensity modulation was necessary to retain the details of the original image in the pseudocolor map. The noise reduction and pseudocolor mapping (detailed in Appendix A) was optimized empirically to provide the best details of the gas (flame) - liquid interactions. It was applied systematically to sequences of images which were then animated and compared to the raw cinematic images.

The color image analysis techniques were initially developed and tested on the cinematic record from Test #29. This record was chosen because both high combustion intensity and excellent visualization were achieved in the test. The high combustion intensity was a result of using a large (1.0 mm) diameter orifice, an above nominal injection velocity, and an above nominal ambient pressure. Figures 22 and 24 show original cinematic images of Test #29, and Figures 23 and 25 show their image enhanced versions. The pseudocolor map in the enhanced versions delineates three major regions in the spray. Blue indicates

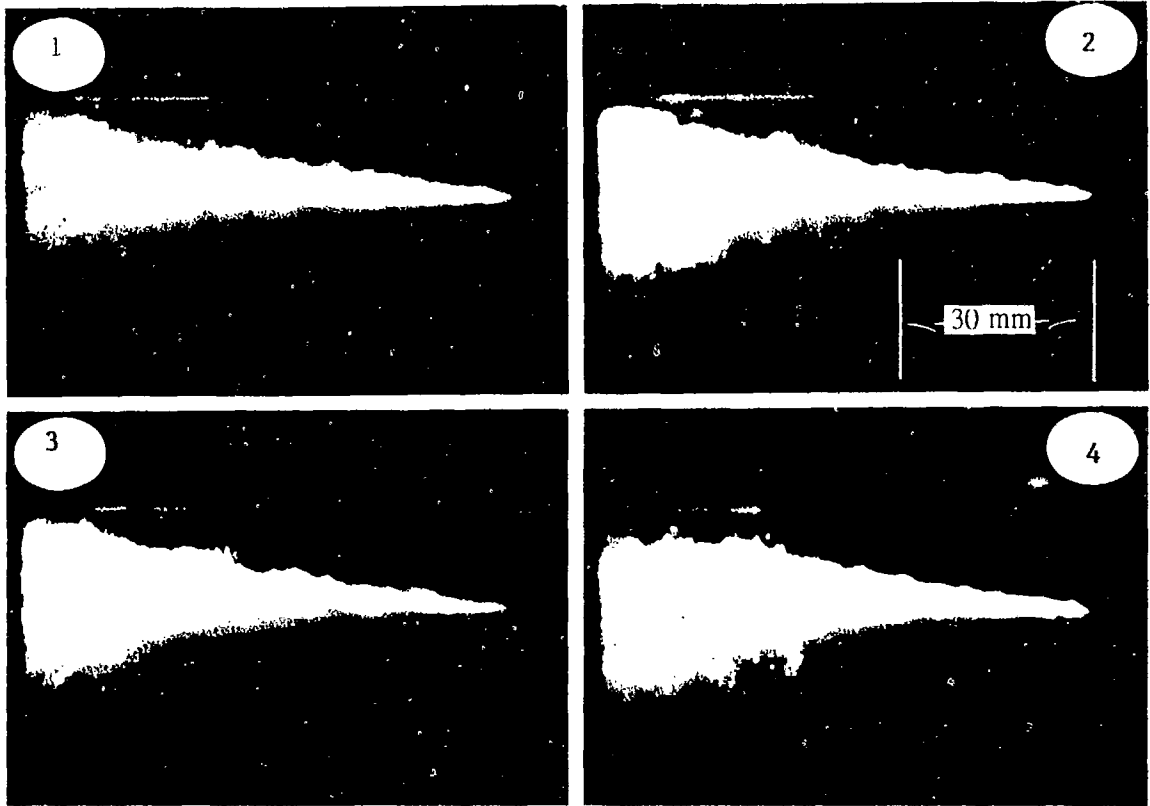


Figure 22. Cinematic Sequence of Progression of 1-mm I.GP1845 Reactants From Ignition to Quasisteady Behavior (Every 3 ms, Test No. 29).

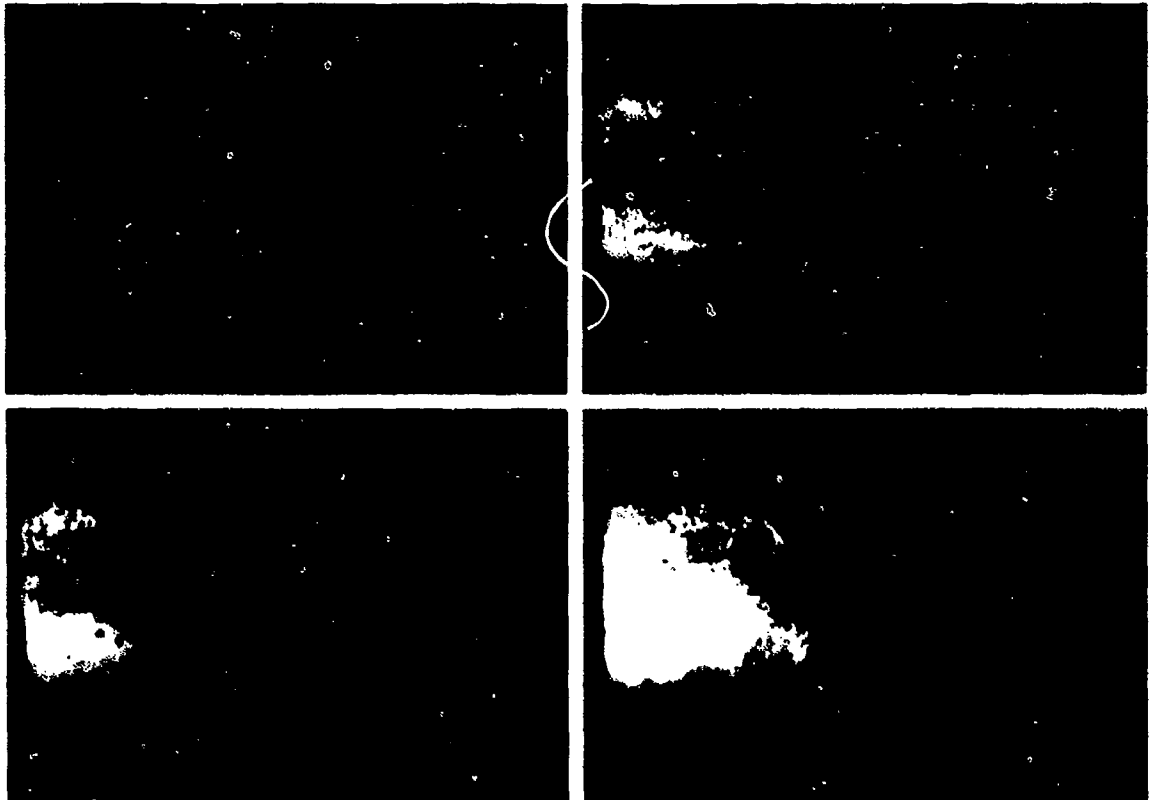


Figure 23. Color Image Analysis of Figure 22 Sequence: Blue - Nonreactant Liquid; Green, Red, Yellow - Increasing Degrees of Reactivity.

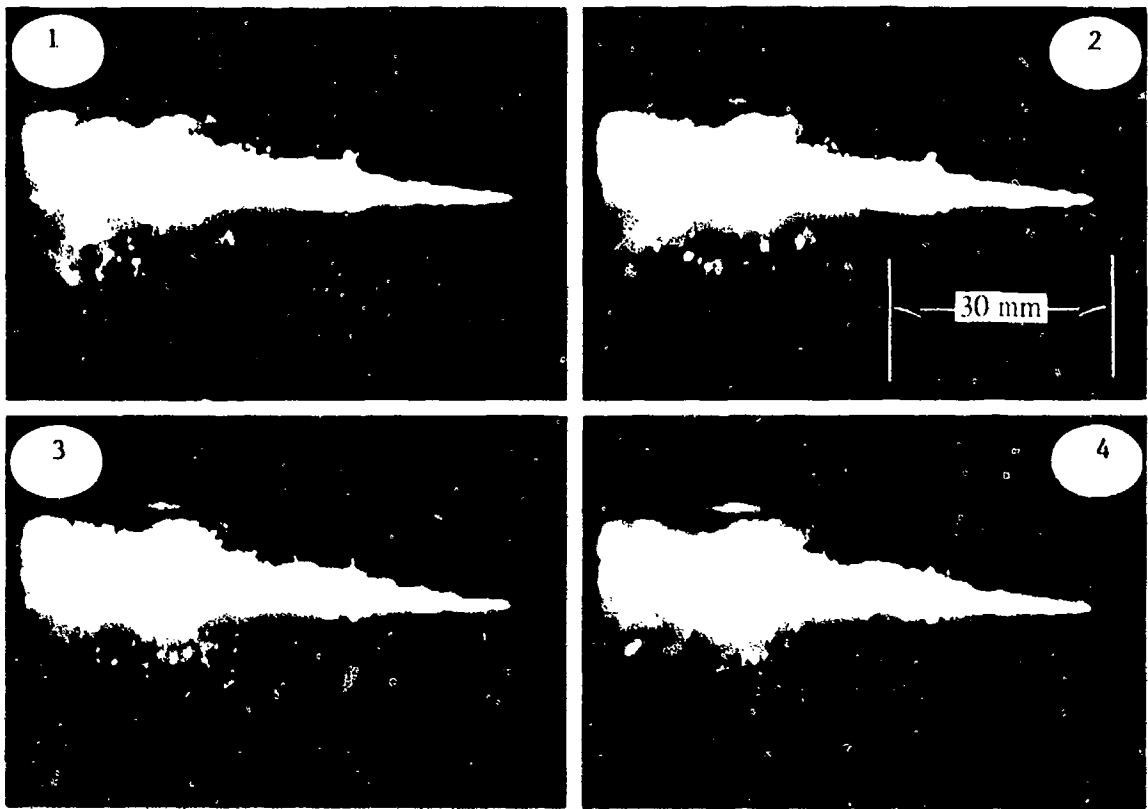


Figure 24. Cinematic Sequence of 1-mm LGP1845 Quasisteady Combustion (5,000 frames/s, Test No. 29).

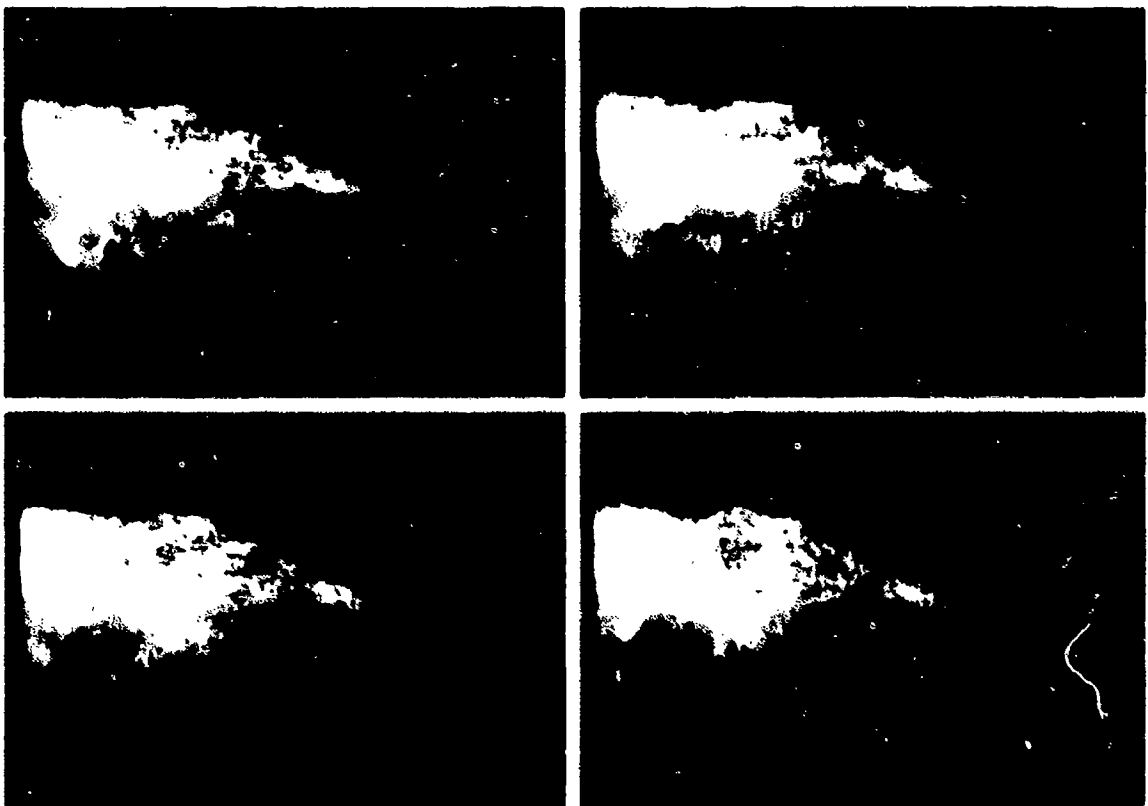


Figure 25. Color Image Analysis of Figure 24 Sequence.

unburned liquid, green indicates a transitional case, and red shading into yellow indicates progressively more energetic combustion where flame emission is most intense. As shown in Figures 22 and 23, ignition started in the far field and flame propagated upstream. In all sequences, burning in vortices is prominent, as is the existence of submillimeter size burning particles. The color image enhancement (Figure 25) of the large burning particles creates green circular specks surrounded by a yellow circle (flame). Thus, liquid particles underlying the flame were revealed via the image processing procedure.

The sequences also show that some features change gradually from frame to frame while others change drastically. For example, some of the drops in Figure 24 and 25 can be followed for several frames while others occur in one frame only. Interestingly, a (solar type) prominence lasts for the entire sequence. These results indicate some coherency in the combustion process. This is particularly evident close to the nozzle.

9. DISCUSSION

9.1 LIQUID JET BREAKUP AND SPRAY FORMATION

Of the mechanisms leading to the combustion of LPG, the rate limiting process is expected to be the breakup and atomization of the LPG jet into small liquid particles. The dynamics of this process, therefore, control the amount of LPG present in the combustion chamber at any given time. If LPG accumulates beyond a threshold amount, the combustion process has the potential to become unstable and prone to pressure fluctuations. The visualization of LPG spray achieved in this study provides a basis for approaching the analysis and modeling of RLPG combustion processes.

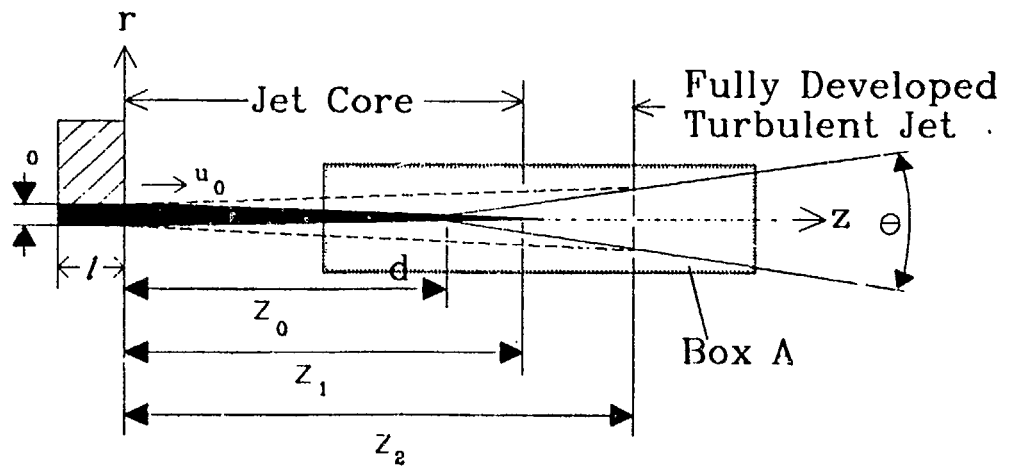
Although in present RLPGs, the LPG is injected through annular orifices, the dynamics of full cone sprays generated from simple circular orifices were investigated in this study. This was done for both practical and scientific reasons. Experiments with circular orifices could be made safer, more controllable, provide longer quasi-steady test conditions, and with better visualization than comparable experiments with annular sprays. Also, the experimental results could be interpreted and compared to the extensive data base which exists for full cone sprays. The database for annular sprays is comparatively small and of questionable value. Admittedly, annular sprays may have some unique characteristics (Birk and Reeves 1987), but fundamental LPG spray combustion dynamics should be the same for these two configurations.

As a case in point, pressure fluctuations have been observed in combustors employing full cone sprays (Rychnovsky et al. 1990).

Numerous models have been proposed to predict the behavior of full cone sprays. After an exhaustive search of the literature, we chose to analyze the present results following the treatment suggested in the elegant review by Bracco (1985). This review considers the full cone spray atomization from simple circular orifices as the two-phase counterpart of single-phase incompressible turbulent jets. The closer the gas density is to the liquid density, such as found at the very high pressure reached in guns, the more physically correct it becomes to consider a spray as a turbulent jet. The review also outlines the use of aerodynamic theory for predicting primary atomization parameters.

A schematic diagram of spray structure and some characteristic parameters are shown in Figure 26. The schematic is appropriate for $\rho_G/\rho_L > 0.1$, the regime in which we are interested. For comparison, the spray structure observed in Test #27, where $\rho_G/\rho_L = 0.334$, is shown. The intact liquid core length (z_1) in the spray corresponds to the potential core length (z_{1i}) in a single-phase turbulent jet. (The intact core length is also referred to as the breakup length.) When the orifice diameter (d_o) and the injection velocity (u_o) are the same for both cases, z_1 is longer than z_{1i} by a factor which is primarily a function of $(\rho_L/\rho_G)^{1/2}$. The turbulent jet reaches a fully developed region called the far field after a development length designated z_{2i} . Similarly, a far field is achieved in a spray ($z_2 > z_{2i}$) in which the spray is dilute and there is no slip velocity between the phases. The velocity and spray concentration profiles are self-preserving in both turbulent jets and sprays. That is, their profiles scale to $r/(z-z_o)$ where r is the radial distance from the centerline and the z_o is the virtual origin of the jet divergence angle θ . The tangent of the divergence angle θ is linearly proportional to a semiempirical constant related to l/d_o multiplied by $(\rho_G/\rho_L)^{1/2}$. The center-line spray velocity decreases with distance as $(\rho_L/\rho_G)^{1/2}/(z-z_o)$, and entrained mass increases as $(\rho_G/\rho_L)^{1/2}(z-z_o)$.

The spray outline in the far field does not form a pure conical shape. Rather it has a jagged envelope and exhibits a high degree of vorticity. Although most information and data relates to the far field, from modeling (Coffee et al. 1991) it is expected that unreacted liquid does not exist much beyond z_1 in gun applications. This conclusion is confirmed in the present work where combustion is shown to occur in the dense spray region delineated by Box A in Figure 26. This region is a transition zone between the near and far fields of the spray. Since the jet breakup and transition zone are most relevant for gun applications, the following discussion focuses on characterization of this region.



Box A

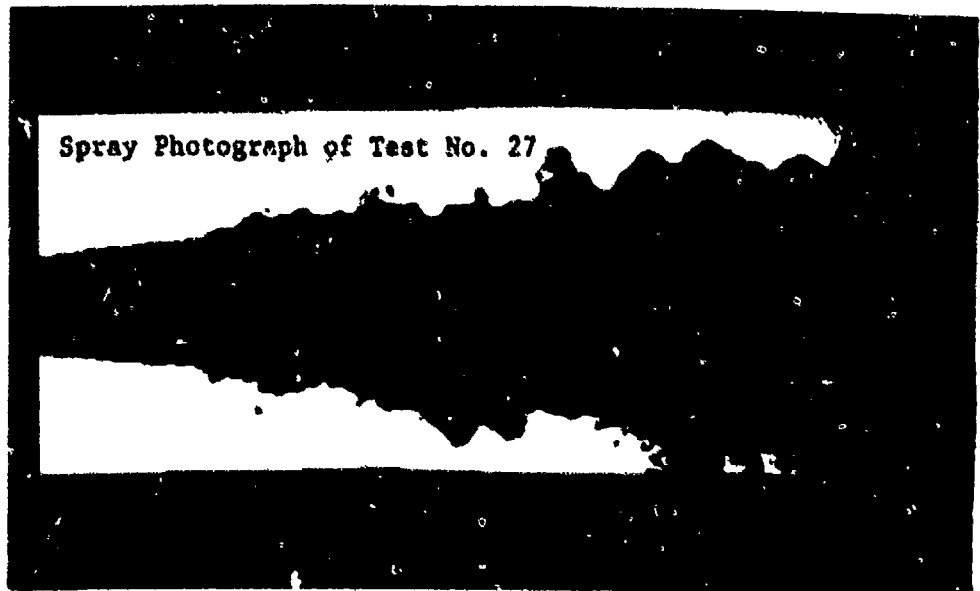
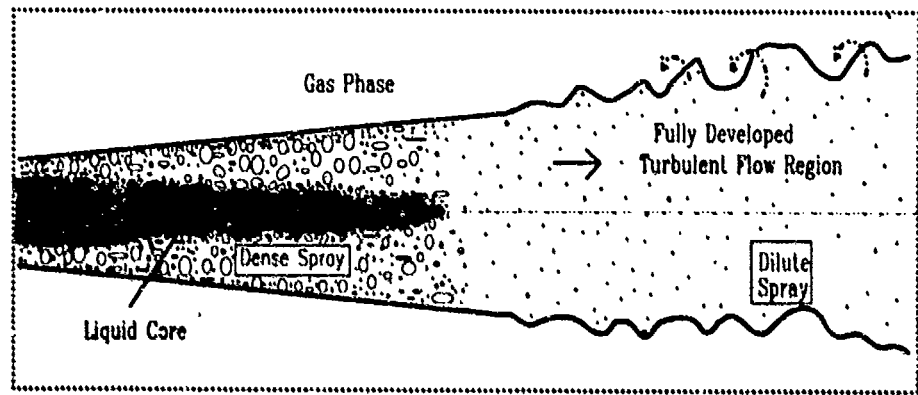


Figure 26. The High Pressure Spray as the Counterpart of a Single-Phase Turbulent Jet.

With respect to atomization processes, the basis for drop formation in the aerodynamic theory is related to disturbances on the core (or on large liquid blobs constituting the core region [Reitz 1987]) which grow unstable due to capillary/aerodynamic forces. The most unstable protuberances detach and form the primary atomization droplets. It should be noted that other mechanisms for jet breakup have been postulated (Bracco 1985). These include "pipe" turbulence in the nozzle, liquid supply pressure oscillations, and cavitation. Of these, only turbulent-induced breakup is a potentially viable atomization mechanism for the experiments presented above. The Reynolds number ($Re_L = \rho_L u_o d_o / \mu_L$) of the flow through the injector nozzle is above the critical value for turbulent flow in pipes (i.e., above 2,000). However, fully developed turbulence was achieved only after $l/d_o > 40$ and the injector nozzles used in this study had l/d_o ratios equal to 4. Thus, the high Re_L flows probably created some degree of turbulence, but the velocity profile of the flow in the exit channel was primarily laminar. (This is particularly true for experiments in which a 0.5-mm-diameter orifice was used.) Therefore, the following comparisons are mainly with respect to the aerodynamic theory.

The values of experimental parameters which are used to predict behavior based on the aerodynamic theory of jet breakup are summarized in Table 3. All tests were within the regime where breakup begins immediately at the injector nozzle exit. Modeling based on the aerodynamic theory provides relationships for predicting the spray angle (θ), intact core length (z_1), and primary drop sizes (d_p) for a given set of test conditions. The values of θ , z_1 , and d_p calculated for the experiments of Table 3 are given in Table 4. The basis for the calculated values and their comparison with the experimental results is as follows.

9.1.1 SPRAY DIVERGENCE ANGLE

For $\rho_G/\rho_L < 0.1$, the spray angle may be calculated from the aerodynamic theory using

$$\tan(\theta/2) = c_0 g(\text{Oh}, \text{We}_G, \text{We}_L) \quad (1)$$

where $\text{Oh} = (\mu_L/\rho_L \sigma d_o)^{1/2}$ is the Ohnesorge number, $\text{We}_L = \rho_L u_o^2 d_o / \sigma$ is the liquid Weber number, and $\text{We}_G = \rho_G u_o^2 d_o / \sigma$ is the gas Weber number. The Ohnesorge number contains the influence of liquid viscosity (μ_L) while the Weber numbers contain the influence of surface tension (σ). (The function g can be found in [Reitz 1987] and the reader is referred to this article for its explicit expression.) The parameter c_0 is an empirical constant related to the nozzle geometry. It depends mainly on l/d_o and the

Table 3. Summary of Test Conditions Related to Atomization^a

	ρ g/cm ³	μ g/cm-sec	σ g/sec ²	ρ_G/ρ_L	Re_L	Re_G	We_G	Oh
LGP1845 ^b	1.47	0.071	67	0.098 ^c	5690	132000	6500	0.045
				0.110 ^d	15500	403000	27100	0.032
Water	1	0.01	72	0.130 ^e	51300	222000	9490	0.0053
Ethanol	0.79	0.011	24	0.160 ^f	54500	313000	58500	0.011
Nitromethane	1.13	0.08	41	0.111 ^g	57800	127000	11400	0.0055

^a Values of Re , We and Oh are based on u_j , d_j .

^b Values for LGP1845 are representative (within 7%) of the LGP1898 and HAN and TEAN water mixtures used.

^c At nominal test conditions (0.5 mm jet injected at 110 m/s into 500°C, 33 MPa).

^d Maximum conditions - 1 mm jet injected at 150 m/s into 500°C, 37 MPa (test number 29).

^e 1 mm jet injected at 103 m/s into 530°C, 31 MPa (test number 28).

^f 1 mm jet injected at 150 m/s into 480°C, 28 MPa (test number 31).

^g 0.5 mm jet injected at 122 m/s into 480°C, 28 MPa (test number 32).

Table 4. Estimated Spray Attributes^a

	θ (Eq. 1) Degrees	θ (Eq. 2) Degrees	θ (Exp.) Degrees	z_1 (Eq. 3) mm	d_p (Eq. 4) μ m
LGP1845	12.7 ^b	16.2	18.5 ^c	16	0.77
	12.9	16.4	18.5	30 ^d	0.97
Water	18.7	16.7	16	28	1
Ethanol	16.4	17.2	12	25	0.17
Nitromethane	16.9	16.4	< 12	15	0.44

^a Corresponding to Table 3 tests.

^b For high speed tests (numbers 17 and 21) $\theta = 11.9$

^c For high speed tests $\theta = 16$. For TEAN test (number 24) $\theta = 17$.

^d For 2mm jet (number 5) $z_1 = 63$ mm.

nozzle entrance profile. For the present case where $l/d_0 = 4$, $c_\theta = 0.19$ is suggested (Reitz 1987). The θ values calculated using Equation 1 range from 12.7° for an LGP test to 18.7° for a water test.

For comparison, we calculated spray angles based on consideration of the spray as a fully developed turbulent jet. Following Abramovich (1963), θ for a fully turbulent jet can be determined using

$$\tan(\theta/2) = 0.13(1 + \rho_G/\rho_L). \quad (2)$$

Unlike Equation 1, this equation is valid for a wide range of ρ_G/ρ_L . Spray angles calculated using Equation 2 fall within a fairly narrow range ($16.7 \pm 0.5^\circ$).

The spray angle could be measured in the present experiments to an accuracy of $\pm 1^\circ$. The comparison of experimentally observed and calculated spray angles does not provide evidence which favors the use of either the aerodynamic theory or the turbulent jet theory to predict spray performance. The water spray angle fits the result from the turbulent theory, and it is in fair agreement with the aerodynamic theory. The trend to smaller angles for higher velocity sprays fits the aerodynamic theory. However, the higher degree of liquid evaporation and decomposition (due to increased heat transfer associated with greater turbulence created by the higher speed) could also account for the smaller angle. Reduced spray angles associated with increased spray reactivity is clearly demonstrated in the supercritically evaporating ethanol and nitromethane sprays. The aerodynamic theory also significantly underpredicts θ for the HAN-based propellant sprays. Based on these results we tentatively conclude that the sprays behave like single phase turbulent jets only in the far field.

9.1.2 BREAKUP LENGTH

Both the aerodynamic theory and available experimental data establish that for $\rho_G/\rho_L < 0.1$, the breakup length is given by

$$z_1 = c_c d_0 (\rho_L/\rho_G)^{1/2}, \quad (3)$$

where c_c is a constant equal to a value between 7 and 16 (Chehroudi, 1985). Calculated values range from approximately 15 mm to 63 mm.

Experimentally, it is very difficult to determine the length of the liquid core using visualization techniques because it is masked by the dense spray region. Although the intact core length could not be measured accurately, the large temperature difference between the (room temperature) injected liquid and the hot ambient gas provided a means for determining if the intact core reached the thermocouple fixed 45 mm above the injector. If the core reached the thermocouple, the temperature readings would have been close to room temperature, and not the $>200^{\circ}$ C readings observed. (See Figure 2.) This approach to characterizing the intact core length may be compared to the established experimental technique of using probes which conduct current when the intact cores act to close an otherwise open electrical circuit. The thermocouple measurements established that in all tests involving 0.5- and 1.0-mm-diameter orifices, z_1 was less than 45 mm. In Test #5, the only experiment utilizing a 2-mm-diameter orifice, z_1 was found to exceed 45 mm. Thus, the experimental results and the z_1 values calculated in Table 4 are consistent. The intact core length is expected to be the parameter least sensitive to evaporation and combustion. Therefore, it is possible that the aerodynamic theory provides reasonable estimates for the jet breakup length.

9.1.3 PRIMARY DROP SIZE DISTRIBUTIONS

When Oh and ρ_G/ρ_L are less than 0.1, primary drop sizes predicted by the aerodynamic theory can be calculated using the simplified relation

$$d_p = c_B d / We_G, \quad (4)$$

where c_B is a constant with a value between 10 and 40. Based on this equation, droplets formed via primary atomization in these tests are expected to have a submicron mean drop diameter. However, it is not possible using currently available experimental techniques to determine primary drop size distributions. Extremely large particles were observed in subcritically reactive sprays, but these are presumably the result of droplet coalescence—a secondary process. This observation highlights the fact that the particle size distribution depends to a large extent on coalescence and secondary breakup processes in the dense spray region. These processes are not considered in the aerodynamic theory; therefore, the aerodynamic theory and its estimates of primary drop size distributions (alone) may not properly represent the actual size distributions in high-pressure sprays.

9.2 SECONDARY ATOMIZATION AND DROPLET COALESCENCE

Submicron-sized drops produced by primary atomization are not expected to last any appreciable distance down the spray. They are prone to elimination by both collisional processes and by rapid evaporation. Assuming uniform size particles, the number of collisions per unit time and volume (\bar{n}_p) is estimated to be (Hinze 1975)

$$\bar{n}_p = \bar{u}_r(1 - \alpha)^2/d_p^4, \quad (5)$$

where \bar{u}_r is the relative mean velocity between the particles and α is the void fraction. Equation 5 expresses the strong dependence of the collision rate on drop size and void fraction. In the dense spray region where the submicron primary drops are formed, the void fraction is close to zero. Therefore, if the liquid is relatively unreactive, the collision rates will be extremely high and drop coalescence will be significant. If evaporation is not significant in the dense zone, larger drops will form whose size will be controlled by secondary breakup processes.

The extent of secondary breakup processes is correlated with the gas Weber number (We_{pG}) and a temporal parameter (t_b). The Weber number above which a drop will break is known as the critical Weber number. Unfortunately, several experimentally determined values have been reported for this parameter and a consensus favoring one has not been reached. We have chosen to follow Clift (1978) in which breakup was found to occur for

$$We_{pG} > We_{pG}^* = 6.5 \quad (6a)$$

where

$$We_{pG} = \rho_G d_p (u_p - u_G)^2 / \sigma. \quad (6b)$$

Following Ranger and Nicholls (1969), the lifetime of a droplet is given by

$$t_b = 4d_p(\rho_L/\rho_G)^{1/2}/(u_p - u_G). \quad (7)$$

If the difference $u_p - u_G$ is known, Equations 6 and 7 can be used to find the largest possible size of stable drops and the lifetime and trajectories of larger drops.

Unfortunately, it is very difficult to approximate $u_p - u_G$. Collisional processes tend to increase the average drop size and, therefore, the drop response to gas motion is very complex. Since the response time of drops to velocity fluctuations is proportional to $d_p/(\rho_G)^{1/2}$ (Faeth 1987), it can be assumed that micron size droplets in dense gas will have no slip velocity. Therefore, the relative velocity will be equal to the local turbulent velocity. For example, if the submicron size primary droplets instantaneously attain local gas velocities, they can coalesce to rather large drops with low values of $u_p - u_G$. Therefore, they will be stable with respect to secondary breakup. Interestingly, if such small drops do exceed We_{PG}^* , Equation 7 implies their lifetime will be very short. Larger drops are more likely to be broken in eddies by local turbulent velocity fluctuations if their breakup time is shorter than the time they spend in the eddies. In Table 5, the critical drop size d_p^* and its breakup time t_b^* are shown vs. a range of $u_p - u_G$ up to 20% of the injection velocity. As the values in Table 5 indicate, drops 0.1 mm and larger are possible in the sprays tested if the local velocity fluctuations are below 5 m/s. Such conditions exist in vortices in the transition and far field regions of the sprays. Indeed, the cinematic records reveal large droplets associated with semi-stationary vortices on the spray boundaries. (See Figures 24 and 25.) Table 5 shows that such droplets could be stable for a few milliseconds.

9.3 THERMAL CONSIDERATIONS - HEAT TRANSFER, EVAPORATION, AND COMBUSTION

In guns, as in the present tests, the injected liquid has a much lower temperature than the ambient gas. As the liquid particles ignite and burn, the spray attains a certain penetration distance which corresponds to the conversion of liquid into gaseous products. (See Figure 8.) This condition is also reached in purely evaporating sprays. Heat transfer processes may not significantly affect the breakup length, but they have a profound effect on the particle sizes of the spray, particularly in the transition and far fields. At supercritical conditions, even the dense spray zone will be significantly affected.

The heat transfer processes in dense sprays are highly complex. They depend on particle size, distribution, number density, turbulence characteristics, and droplet trajectories. The most conservative calculation of the time (t_h) it takes to heat a droplet a certain ΔT_1 is obtained by assuming no heat transfer augmentation due to convection, and by considering the droplet temperature to be uniform. For this case, t_h may be approximated using

$$t_h = \rho_L c_{PL} d_p^2 \Delta T_1 / 12 K_G \Delta T_2 \quad (8)$$

Table 5. Critical Drop Size and Secondary Breakup Times for LGP1845^a

$u_p - u_G$ m/s	1	2	5	10	20
d_p^* μm	3018	755	121	30	7.5
t_b^* msec	38.65	4.83	0.309	0.039	0.0048

^a At nominal test conditions.

where ΔT_2 is the average temperature difference between the gas and the liquid, K_G is heat conductivity of the gas, and c_{pL} is the specific heat capacity of the liquid. For the present test conditions, $\Delta T_1 = 200^\circ \text{C}$, and we assume $\Delta T_2 = 2\Delta T_1 = 400^\circ \text{C}$. Using values of $K_G = 0.00026 \text{ cal/cm-K-s}$ for nitrogen and $c_{pL} = 0.57 \text{ cal/g-K}$ for LGP1845, Equation 8 yields $t_h = 0.001, 0.003, 0.034, 0.13, 0.54 \text{ ms}$ for $d_p = 1, 2, 5, 10, 20 \mu\text{m}$, respectively. Assuming a drop velocity equal to the injection velocity of 110 m/s , a $1\text{-}\mu\text{m}$ droplet (from primary atomization as per Table 3) will traverse 0.1 mm during a typical heat-up to 200°C . Thus, small droplets formed via primary atomization in the hot ambient gas on the periphery of the dense zone will reach high temperature in very close proximity to their detachment points from the liquid core.

In supercritically evaporating sprays (Tests #30, #31, and #32), the lifetime of such droplets may be so short as to preclude the formation of a dense spray region. Furthermore, supercritical conditions hinder the coalescence of primary atomization droplets because surface tension rapidly decreases as the liquid approaches its critical temperature. Thus, the liquid core breakup at such conditions may not result in spray at all. This is likely the situation depicted in Figure 18. This situation is in contrast to subcritical conditions where the average drop size may increase markedly due to coalescence. In the case of LGP, coalescence may occur well before drops reach their decomposition or ignition temperature. This produces slower drop heating rates and postpones ignition to regions beyond the dense spray zone.

As already discussed, the entrained gas mass in sprays grows very rapidly downstream of the virtual origin of the spray. At the point where the temperature is measured in the present tests (about 45 mm from the injector), it is estimated, based on the spray angles, that the ratio of the entrained gas to liquid masses is well over 10. Because the heat capacity of the gas per unit mass is close to that of the liquid, the entrained gas has sufficient capacity to heat the liquid close to the local ambient gas temperature.

Based on the thermocouple measurements (Figure 2) and drop heating times (t_h) calculated above, it seems likely that the sprays are homogeneous at the measurement location. If this is the case, then the temperatures measured are indicative of the local liquid temperature.

This observation is interesting in view of the proposed scheme for LGP1845 spray combustion (Carleton et al. 1990). In this scheme, combustion is assumed to occur in stages which start with the decomposition of HAN into nitric acid, NO_x , N_2 , and water at about 120°C . This process is only mildly exothermic. When the nitric acid reaches 180°C , it decomposes into NO_2 and OH , which react promptly and exothermally with the TEAN. Significant reaction (re: sustained ignition) is not expected until the temperature reaches this point.

In view of this scheme, we found it surprising that the temperature measured inside the spray was above the nitric acid decomposition temperature (Figure 2), yet well below flame temperature, even when flame was enveloping the spray. Furthermore, the measured HAN spray angles (Table 3) indicate that little decomposition occurred until well downstream of the thermocouple. Taking into account the characteristic heating times calculated earlier, significant decomposition on the periphery of the HAN sprays was expected. This would have resulted in much smaller spray angles than those measured. It is, therefore, surmised that even at 250°C and 33 MPa, the decomposition kinetics of the HAN is relatively slow (Figure 2). In these experiments, the rate of heat transfer from the entrained ambient gas to the spray determines the ignition location in the spray. If the temperatures inside the spray are not high enough to rapidly decompose HAN and HNO_3 , the decomposition products will be diluted by the entrained inert ambient gas and combustion will not be complete.

Comparison of the tests results for the LGP1845 and LGP1898 sprays also indicates that, in addition to a temperature threshold, the LGP sprays require some threshold concentration of reactive species before significant reaction occurs. The LGP1898 uses DEHAN instead of TEAN for a fuel component (Klein et al. 1991). The DEHAN decomposition temperature is similar to that of the HAN and, therefore, HAN and DEHAN decompose almost simultaneously. This results in a prompter, more vigorous reaction than achieved with the LGP1845 under the conditions of these experiments.

The test results also demonstrate the impact of general turbulence on the periphery of the spray in the transition and far field regions. Turbulence enhances heat transfer and the mixing of reactive species in these regions. It was always observed that ignition first occurred in the far field. Flame advancement

towards the transition region was associated with turbulent recirculation of the gas. (Turbulent recirculation of the gas is a result of injecting into a closed chamber.) Also, evaporation/combustion acts to redistribute axial momentum in the radial direction. Coupled with the turbulent recirculation, this facilitates flame advancement up the spray by seeding the spray with reactive species.

The cinematic records clearly indicate vortex formation on the spray envelope. The long residence time of liquid particles in vortices facilitates ignition and sustained burning in this area. The cinematic records also indicate that the large drops (hundreds of microns in size) were associated with the vortices. The mechanism of the formation of these large droplets is not well understood, but it is hypothesized that the drops are produced by the coalescence of much smaller drops in converging stream lines in the vortices. The slip velocities in vortices are sufficiently low that the secondary breakup of the drops is precluded. The photographic records indicate apparent burning rates for the large drops of 10 to 100 cm/s, regardless of LGP type. These rates are only rough estimates, but they are in the range found in previous studies (Lee et al. 1990). Another observation is that the formation process of the large drops apparently induced occasional magnus forces on droplets, causing abrupt and random changes in their trajectories. Once the large drops accelerated, secondary breakup took place and the fragments were consumed by combustion.

The supercritically evaporating sprays exhibited unique characteristics. The photographic evidence indicates intermittent breakup of blobs from the tip of the liquid core. The blobs, apparently composed of densely packed small particles, expand and swell downstream before completely evaporating. It is possible that the swelling, rather than indicating radial droplet velocities (as in conventional subcritical sprays) is a manifestation of rapidly decreasing density as the liquid particles approach their critical temperature. The structure and behavior of supercritically evaporating sprays are still poorly understood. Presumably, the behavior of supercritical combusting sprays resembles that of supercritical evaporating sprays.

9.4 IMPLICATIONS OF THE PRESENT WORK TO MODELING OF COMBUSTION IN GUNS

Recent effort has been devoted to modeling the pressure fluctuations prevalent in RLPGs. Coffee (1992) has been successful in numerically simulating coherent pressure oscillations associated with acoustic modes. In his model, the liquid is injected with a known average Sauter mean diameter drop size. Having specified the initial burning area and a pressure-dependent burn rate, the evolution of the spray

is followed using the LHF approximation. (This approximation assumes no slip velocity between the two phases.) When a steep pressure dependency of the burn rate is assumed ($d d_p/dt \sim p^n$, $n > 1.2$), pressure oscillations develop due to wave reflection from the chamber walls. One shortcoming of this model is that it does not consider liquid core breakup processes. Such processes are certainly important. Equation 3 indicates that liquid core size will decrease with pressure. Therefore, a transverse pressure wave may break a large section of the liquid core into rapidly burning segments. Also, the validity of the burn rate pressure dependence used in the model is at present tentative. In principle, a model can be devised which considers the interaction of the liquid core with transverse pressure oscillations while assuming a much milder dependency of burning rate on pressure. While such a jet breakup model would be more physically realistic, experimental data useful for validating such a model is lacking.

The combustion in these experiments occurs at subcritical conditions and the amount of propellant burning in large drops appears to be a large fraction of the total. Even so, the present work establishes that combustion on the periphery of the sprays can take place within $z/d_0 = 20$ of the injector. This corresponds to the dense spray region (Figure 26). The ambient temperatures and pressures during most of an interior ballistic cycle are much higher than those studied in these experiments and, at pressures above 60 MPa, the combustion in guns may be supercritical (Kounalakis and Faeth 1988). At gun temperatures and pressures, reactions would accelerate such that droplets formed via primary atomization might not have time to coalesce into large droplets. Supercritical conditions would further render large droplets unstable due to reduced surface tension. These considerations suggest that burning sprays in guns will be consumed a short distance from the liquid core and a far field region will not develop. Also, the combustion, whether subcritical or supercritical, is likely to be highly turbulent with sizable local fluctuations. At the high pressures in guns where the combustion intensities are extremely high, it is possible that turbulent fluctuations could generate high local pressures. These could then be echoed by adjacent chamber walls and reinforced. The LGP1845/nitromethane test (#33) indicates that large LOP drops can be formed even when ambient gas temperatures are higher than the 500° C obtained with heated nitrogen alone. However, more definitive studies are required to characterize the competing processes of secondary atomization and droplet coalescence at high temperatures.

Until data is available regarding the structure and pressure dependency of burning rates in sprays at pressures above 60 MPa, it is suggested that modeling of separated flow phenomena, such as droplet trajectories in the far fields of sprays, be avoided. Modeling should instead concentrate on the breakup process of the liquid core since the core exists for both subcritically and supercritically combusting LOP

sprays. Existing models of liquid core breakup in sprays apply turbulent theories such as the LHF approximation (Faeth 1987), the aerodynamic theory (Reitz 1987) and the jet embedding technique (Przekwas et al. 1988). At this time, the LHF approximation has not yet been attempted in gun codes, and a partial use of correlations based on the aerodynamic theory of jet breakup was unsuccessful (Coffee et al. 1991). The present work shows that in dense sprays drop coalescence and secondary breakup processes are very important if the sprays burn subcritically. Computer codes developed to account for such processes may be prohibitively time consuming to run. Thus, it may not be desirable to attempt to model the results of this experimental study. In contrast, an LHF-based code suitable for spray conditions at the high temperatures and pressures in a gun should be far easier to implement. Even so, it is important to remember that the physical basis of the established theories have weak points and all include questionable empirical parameters. It should also be remembered that the injection nozzles in most RLPG are annular and have complex exit channel geometries. The adaptation of the aerodynamic theory to these cases is not straightforward.

Future testing with the existing facility will be undertaken to establish liquid core lengths of both full circular and annular simulant jets through the use of soft x-ray photography. However, the study of pressure fluctuations and their interaction with the core will not be possible due to the low pressure rating and the limited combustion intensities which can be achieved. A 150-MPa spray-combustion visualization facility which addresses these shortcomings is now under design. This facility will reveal whether the LGP burns supercritically at pressures where pressure oscillations are found in guns.

10. CONCLUSIONS

- 1) In the pressure range tested (i.e., <40 MPa), the combustion of HAN-based LGP sprays is subcritical.
- 2) Subcritical combustion of LGP sprays at high pressures is controlled by turbulent mixing processes and occurs in vortices enveloping dense spray in the transition region between the near field (liquid core break-up) and the far field (fully developed turbulent jet).
- 3) Drop coalescence in vortices results in a significant percentage of the LGP burning as large (ca. 1 mm) particles. The small burning area to volume ratio for these particles can increase the level of

unreacted LGP in the RLPG combustion chamber and render the combustion more susceptible to pressure fluctuations.

4) The experiments with nitromethane and ethanol demonstrate that supercritical combustion is likely to be controlled by liquid core break-up dynamics. Spray particles will be extremely small and combustion will be complete in close proximity to the core. Pressure fluctuations may interact strongly with liquid core dynamics.

5) Subcritical combustion of LGP was observed to occur in the transition region. This indicates that even if combustion at high gun pressures is still subcritical, combustion is likely to be complete within a few centimeters beyond the liquid core.

6) The highly turbulent and random nature of the combustion observed in this study indicates a mechanism whereby local pressure excursions can be triggered. However, as no pressure oscillations were observed, the present work does not establish a mechanism for their sustained growth.

7) If the mechanisms driving pressure fluctuations in RLPG's are to be unequivocally determined, experiments will have to be extended to pressures above 100 MPa. The visualization techniques presently developed are applicable to such elevated pressures.

INTENTIONALLY LEFT BLANK.

11. REFERENCES

- Abramowitz, G. N. The Theory of Turbulent Jets, M.I.T. Press, 1963.
- Baier, G. R. "Analytical and Experimental Analysis of Liquid Propellant Injection and Ignition at High Pressures." Master of Engineering Dissertation, Rensselaer Polytechnic Institute, Troy, NY, May 1986.
- Birk, A., and P. Reeves. "Annular Liquid Propellant Jets -Injection, Atomization, and Ignition." BRL-TR-2780, U.S. Army Ballistic Research Laboratory, Aberdeen Proving Ground, MD, March 1987.
- Birk, A., and P. Reeves. "Facility for Visualization of Liquid Propellant Spray Combustion at High Pressures." BRL-MR-3684, U.S. Army Ballistic Research Laboratory, Aberdeen Proving Ground, MD, July 1988.
- Birk, A., and G. Bliessner. "Laboratory Injector for Spray Studies Related to Liquid Propellant Gun." BRL-TR-3209, U.S. Army Ballistic Research Laboratory, Aberdeen Proving Ground, MD, February 1991.
- Boyer, N. E. Private communication, U.S. Army Ballistic Research Laboratory, Aberdeen Proving Ground, MD, April 1992.
- Bracco, F. V. "Modeling of Engine Sprays." SAE Paper 850394, 1985.
- Carleton, F. B., N. E. Klein, K. Krallis, and F. J. Weinberg. "Laser Ignition of Liquid Propellant." Proceedings of the 23rd International Symposium on Combustion, 1990.
- Chehroudi, B., Y. Onuma, S. -H Chen, and F. V. Bracco. "On the Intact Core of Full-Cone Sprays." SAE Paper 850126, 1985.
- Clift, R., J. R. Grace, and M. E. Weber. Bubbles, Drops, and Particles. Academic Press, NY, p. 346, 1978.
- Coffee, T. P. "An Updated Lumped Parameter Code for Regenerative Liquid Propellant In-Line Guns." BRL-TR-2974, U.S. Army Ballistic Research Laboratory, Aberdeen Proving Ground, MD, December 1988.
- Coffee, T. P., G. P. Wren, and W. F. Morrison. "A Comparison Between Experiment and Simulation for Concept VIC Regenerative Liquid Propellant Guns. I. 30 mm." BRL-TR-3072, U.S. Army Ballistic Research Laboratory, Aberdeen Proving Ground, MD, December 1989.
- Coffee, T. P., G. P. Wren, and W. F. Morrison. "A Comparison Between Experiment and Simulation for Concept VIC Regenerative Liquid Propellant Guns. II. 105 mm." BRL-TR-3093, U.S. Army Ballistic Research Laboratory, Aberdeen Proving Ground, MD, April 1990.
- Coffee, T. P., P. G. Baer, W. F. Morrison, and G. P. Wren. "Jet Breakup and Combustion Modeling for the Regenerative Liquid Propellant Gun." BRL-TR-3223, U.S. Army Ballistic Research Laboratory, Aberdeen Proving Ground, MD, April 1991.

- Coffee, T. P. "A Two-Dimensional Model for the Combustion Chamber/Gun Tube of a Concept VIC Regenerative Liquid Propellant Gun." BRL-TR-3341, U.S. Army Ballistic Research Laboratory, Aberdeen Proving Ground, MD, May 1992.
- DeSpirito, J., N. E. Boyer, J. D. Knapton, and A. W. Johnson. "Pressure Oscillation Reduction in a 30 mm Concept VIV RLPG." 28th JANNAF Combustion Meeting, San Antonio, TX, October 1991.
- Faeth, G. M. "Mixing, Transport, and Combustion in Sprays." Progress in Energy Combustion Science, vol. 13, pp. 293-345, 1987.
- Graham, A. R. "The Implication of Combustion Instability in Regenerative Liquid Propellant Guns." 4th International Gun Propellant Symposium, Dover, NJ, November 1988.
- Haberl, J. B. GE/BRL Working Meeting - LP Gun #2 Pressure Oscillations 1992.
- Handbook of Physics and Chemistry, 66th (Ed.), R.C. Weast ed., CRC Press Inc., Boca Raton, FL, 1986.
- Hinze, J. O. "Turbulent Fluid and Particle Interaction." Prog. Heat Mass Transfer, vol. 6, p. 433, 1972.
- Klein, N., T. P. Coffee, and S. C. Lever. "The Effect of Molecular Structure on the Burning Characteristics of the HAN-Based Propellants." 28th JANNAF Combustion Meeting, San Antonio, TX, October 1991.
- Knapton, J. D., and T. C. Minor. "Pressure Waves in Chemical Propulsion Systems." 27th JANNAF Combustion Meeting, Cheyenne, WY, November 1990.
- Kolb, C. E., D. R. Worsnop, M. S. Zahniser, and G. N. Robinson. "Chemical Kinetics and Dynamics of the Mesospheric Sodium Nightglow." 4th Chemical Congress of North America/ 202nd National Meeting of the American Chemical Society, 1991.
- Kounalakis, M. E., and G. M. Faeth. "Combustion of Han-Based Liquid Monopropellants Near The Thermodynamic Critical Point." Combustion and Flame, vol. 74, no. 2, pp. 179-192, November 1988.
- Lee, T. -W., J. P. Gore, G. M. Faeth, and A. Birk. "Analysis of Combusting High Pressure Monopropellant Sprays." Combustion Science and Technology, vol 57, no. 4, pp. 95-112, 1988.
- Lee, T. -W., L. -K. Tseng, and G. M. Faeth. "Separated Flow Considerations for Pressure Atomized Combusting Monopropellant Sprays." Journal of Propulsion and Power, vol. 6, no. 4, pp. 383-391, 1990.
- Lee, T. -W, and G. M. Faeth. "Structure and Mixing Properties of Combusting Monopropellant Sprays." Journal of Propulsion and Power, vol. 8, no. 6, pp. 271-279, 1992.
- Messina, A. N., M. Tarczynski, and S. L. Ingram. "Flow-Induced Shear Heating of Liquid Propellant." 27th JANNAF Combustion Meeting, Cheyenne, WY, November 1990.
- Przekwas, A. J., S. G. Chuech, and K. W. Gross. "Computational Modeling Development for Liquid Propellant Atomization." 25th JANNAF Combustion Meeting, Huntsville, AL, October 1988.

- Ranger, A. A., and J. A. Nicholls. "Aerodynamic Shattering of Liquid Drops." AIAA Journal, vol. 7, no. 2, pp. 285-290, 1969.
- Reitz, R. D. "Modeling Atomization Processes in High-Pressure Vaporizing Sprays." Atomization and Spray Technology, vol. 3, pp. 309-337, 1987.
- Ruff, G. A., P. -K. Wu, L. P. Bernal, and G. M. Faeth. "Continuous and Disperse Phase Structure of Dense Nonevaporating Pressure-Atomized Sprays." Journal of Propulsion and Power, vol. 8, no. 2, pp. 280-289, 1992.
- Rychnovsky, R. E., R. W. Carlin, S. K. Griffiths, S. R. Vosen, and R. F. Renzi. "Reduction of Pressure Oscillations in Liquid Propellant Combustion." 27th JANNAF Combustion Meeting, Cheyenne, WY, November 1990.
- Watson, C. A. "Pressure Oscillations in Regenerative Liquid Propellant Guns." 1989 JANNAF Propulsion Meeting, Cleveland, OH, May 1989.
- Watson, C., J. D. Knapton, and N. E. Boyer. "Effects of Injector Exit Geometry on Pressure Oscillations in 30 mm Regenerative Liquid Propellant Guns." 26th JANNAF Combustion Meeting, Pasadena, CA, October 1989.
- Wren, G. P., T. P. Coffee, and W. F. Morrison. "A Comparison Between Experiment and Simulation for Concept VIC Regenerative Liquid Propellant Guns. III. 155 mm." BRL-TR-3151, U.S. Army Ballistic Research Laboratory, Aberdeen Proving Ground, MD, September 1990.

INTENTIONALLY LEFT BLANK.

APPENDIX:

COLOR IMAGE PROCESSING

INTENTIONALLY LEFT BLANK.

Once an image is ported to the Silicon Graphics Personal Iris 4D20G, it is converted to an RGB image file and placed in an RGB framebuffer in ".pic" format. The RGB image file created from a video frame typically has about 133,000 pixels. Each pixel contains three color components: red, green, and blue. Each color component has an 8-bit dynamic range (i.e., an intensity value from 0 to 255). These components can be separated into individual frame buffers and operated on as appropriate, based on objective criteria for color sources in the original image. It is this feature, three component bit mapping, that allows manipulation of the color content in an image on a pixel by pixel basis.

For the present study, the first step in processing an image involved the elimination of color noise. The characterization of noise levels was done empirically by sampling background regions in the image which should have been black (i.e., $I(R) = I(G) = I(B) = 0$). Based on this survey, threshold values for $I(R)$, $I(G)$, and $I(B)$ or their sum were set to a limiting value below which a pixel element was mapped to black. The threshold values were then adjusted by trial and error until the background was clear with the threshold(s) set as low as possible. Threshold values of $I(G) < 50$ and $I(R) < 32$ were typical. Some enhancement of image detail was achieved by this thresholding procedure.

The second step in processing an image involved calculating the ratio $M=I(R)/I(B)$ and the total pixel intensity $I(T)=I(R)+I(G)+I(B)$ for each pixel not mapped to black. For high values of M ($M > 5$), pixel color components were mapped to: $I(R)=255$, $I(G)=0.63*I(T)$, $I(B)=0$. This results in an output color ranging from red to yellow, with yellow signifying input pixels having the highest value for M . Since this mapping is for high $I(R)/I(B)$ ratios, yellow also corresponds to the highest flame intensity. For $1 \leq M \leq 5$ the input pixel was mapped to: $I(R)=0$, $I(G)=0.63*I(T)$, $I(B)=0$. This mapping gives shades of green. The value 0.63 was found to result in the best detail contrast in the processed image. For $M < 1$ and $I(B) > 50$, the input pixel was mapped to: $I(R)=0$, $I(G)=(0.63 * I(T)+64)/2$, $I(B)=0.63*I(T)+64$. This resulted in a green-tinted bright blue color which printed well on the color video printer (Sony, Model UP-5000). This process resulted in pseudocolor mapping of reactivity without significant loss of image detail related to total intensity variation.

INTENTIONALLY LEFT BLANK.

LIST OF SYMBOLS

- C_B - constant related to primary drop size
- C_C - constant related to liquid core length
- C_p - specific heat at constant pressure, cal/g-k
- C_θ - constant related to spray angle
- d - liquid blob diameter, cm
- d_o - nozzle exit diameter, cm
- d_p - liquid drop diameter, cm
- K - heat conductivity, cal/cm-k-sec
- l - nozzle length, cm
- \dot{n}_p - particle collision rate, 1/cm³-sec
- Oh - Ohnesorge number
- P - pressure, MPa
- Re - Reynold number
- r_1 - radial distance on spray, cm
- T - temperature, °K
- t - time, sec
- t_b - droplet breakup time, sec
- t_h - heat-up time of droplet, sec
- u - velocity, m/sec
- u_o - injection velocity, m/sec
- u_r - relative mean velocity between particles, m/sec
- We - Weber number
- z - axial distance on spray, cm

ρ - density, g/cm³

μ - viscosity, g/cm-sec

σ - surface tension, g/sec²

θ - spray angle, deg

α - void fraction of liquid in spray

SUBSCRIPTS

G - gas

L - liquid

P - particle (droplet)

SUPERSCRIPT

***** - critical value

<u>No. of Copies</u>	<u>Organization</u>	<u>No. of Copies</u>	<u>Organization</u>
2	Administrator Defense Technical Info Center ATTN: DTIC-DDA Cameron Station Alexandria, VA 22304-6145	1	Commander U.S. Army Missile Command ATTN: AMSMI-RD-CS-R (DOC) Redstone Arsenal, AL 35898-5010
1	Commander U.S. Army Materiel Command ATTN: AMCAM 5001 Eisenhower Ave. Alexandria, VA 22333-0001	1	Commander U.S. Army Tank-Automotive Command ATTN: ASQNC-TAC-DIT (Technical Information Center) Warren, MI 48397-5000
1	Director U.S. Army Research Laboratory ATTN: AMSRL-D 2800 Powder Mill Rd. Adelphi, MD 20783-1145	1	Director U.S. Army TRADOC Analysis Command ATTN: ATRC-WSR White Sands Missile Range, NM 88002-5502
1	Director U.S. Army Research Laboratory ATTN: AMSRL-OP-CI-A, Tech Publishing 2800 Powder Mill Rd. Adelphi, MD 20783-1145	1	Commandant U.S. Army Field Artillery School ATTN: ATSF-CSI Ft. Sill, OK 73503-5000
2	Commander U.S. Army Armament Research, Development, and Engineering Center ATTN: SMCAR-IMI-I Picatinny Arsenal, NJ 07806-5000	(Class. only) 1	Commandant U.S. Army Infantry School ATTN: ATSH-CD (Security Mgr.) Fort Benning, GA 31905-5660
2	Commander U.S. Army Armament Research, Development, and Engineering Center ATTN: SMCAR-TDC Picatinny Arsenal, NJ 07806-5000	(Unclass. only) 1	Commandant U.S. Army Infantry School ATTN: ATSH-CD-CSO-OR Fort Benning, GA 31905-5660
1	Director Benet Weapons Laboratory U.S. Army Armament Research, Development, and Engineering Center ATTN: SMCAR-CCB-TL Watervliet, NY 12189-4050	1	WL/MNOI Eglin AFB, FL 32542-5000 <u>Aberdeen Proving Ground</u>
(Unclass. only) 1	Commander U.S. Army Rock Island Arsenal ATTN: SMCRI-TL/Technical Library Rock Island, IL 61299-5000	2	Dir, USAMSAA ATTN: AMXSY-D AMXSY-MP, H. Cohen
1	Director U.S. Army Aviation Research and Technology Activity ATTN: SAVRT-R (Library) M/S 219-3 Ames Research Center Moffett Field, CA 94035-1000	1	Cdr. USATECOM ATTN: AMSTE-TC
		1	Dir, ERDEC ATTN: SCBRD-RT
		1	Cdr, CBDA ATTN: AMSCB-CI
		1	Dir, USARL ATTN: AMSRL-SL-I
		10	Dir, USARL ATTN: AMSRL-OP-CI-B (Tech Lib)

<u>No. of Copies</u>	<u>Organization</u>
1	OSD/SDIO/IST ATTN: Dr. Len Caveny Pentagon Washington, DC 20301-7100
1	Commander (Code 3247) Naval Weapons Center Guns Systems Branch China Lake, CA 93555-6000
1	Commander U.S. Army Materials Technology Laboratory ATTN: SLCMT-MCM-SB, M. Levy Watertown, MA 02172-0001
1	Commander U.S. Army Belvoir Research and Development Center ATTN: STRBE-WC, Technical Library Vault B-315 Fort Belvoir, VA 22060-5606
1	Commander U.S. Army Research Office ATTN: Technical Library P.O. Box 12211 Research Triangle Park, NC 27709-2211
5	Commander U.S. Army Armament Research, Development, and Engineering Center ATTN: SMCAR-AEE, A. Benati J. Lanon J. Salo D. Chiu SMCAR-AEE-B, D. Downs Picatinny Arsenal, NJ 07806-5000
4	Commander U.S. Army Armament Research, Development, and Engineering Center ATTN: SMCAR-FSA, H. Liberman SMCAR-FSS-DA, Bldg. 94, J. Feneck R. Kopman J. Irizarry Picatinny Arsenal, NJ 07806-5000

<u>No. of Copies</u>	<u>Organization</u>
1	OLAC PL/RKFA ATTN: Doug Talley Edwards FB, CA 93524
1	Director Jet Propulsion Laboratory ATTN: Technical Library 4800 Oak Grove Drive Pasadena, CA 91109
1	Director Jet Propulsion Laboratory Chemical Processes Group Propulsion Systems Section ATTN: D.P. Maynard, Technical Group Supervisor 4800 Oak Grove Drive Pasadena, CA 91109
1	Director National Aeronautics and Space Administration ATTN: MS-603, Technical Library 21000 Brookpark Road Lewis Research Center Cleveland, OH 44135
1	Director Sandia National Laboratories ATTN: R. Rychanovsky, Division 8152 P.O. Box 696 Livermore, CA 94551-0969
1	Director Sandia National Laboratories ATTN: R. Carling, Division 8357 P.O. Box 696 Livermore, CA 94551-0969
1	Director Sandia National Laboratories ATTN: S. Griffiths, Division 8244 P.O. Box 696 Livermore, CA 94551-0969
1	Director Applied Physics Laboratory The Johns Hopkins University 11815 Hopkins Road Laurel, F.D. 20707

<u>No. of Copies</u>	<u>Organization</u>	<u>No. of Copies</u>	<u>Organization</u>
1	The Johns Hopkins University Department of Mechanical Engineering ATTN: Prof. Joseph Katz 118 Latrobe Baltimore, MD 21218	1	Conway Enterprises ATTN: Prof. Alistair MacPherson 499 Pine Top Trail Bethlehem, PA 18017-1828
2	Princeton Combustion Research Laboratories, Inc. ATTN: Neale A. Messina Dr. Martin Summerfield Princeton Corporate Plaza 11 Deerpark Dr., Bldg. IV, Suite 119 Monmouth Junction, NJ 08852	1	CFD Research Corporation ATTN: Dr. Andrzej J. Przekwas 3325-D Triana Blvd. Huntsville, AL 35805
1	Calspan Corporation ATTN: Technical Library P.O. Box 400 Buffalo, NY 14225-0400	1	University of Colorado at Boulder Dept. of Mechanical Engineering ATTN: Dr. John Daily Engineering Center ME 1-13 Campus Box 427 Boulder, CO 80309-0427
7	General Electric Ordnance System Division ATTN: J. Mandzy, OP43-2202 R.E. Mayer W. Pasko R. Pate I. Magoon D. Bair L. Walter 100 Plastics Ave. Piusfield, MA 01201-3698	1	University of California, Irvine Office of the Dean School of Engineering ATTN: Prof. William A. Sirignano Irvine, CA 92717
1	General Electric Company Armament Systems Department ATTN: D. Maher Burlington, VT 05401	1	Pennsylvania State University Department of Mechanical Engineering ATTN: Prof. K. Kuo University Park, PA 16802
1	Veritay Technology, Inc. ATTN: E.B. Fisher 4845 Millersport Highway P.O. Box 305 East Amherst, NY 04051-0305	2	The Johns Hopkins University/CPIA ATTN: T. Christian Technical Library 10630 Little Patuxent Parkway, Suite 202 Columbia, MD 21042-3200
1	Paul Gough Associates, Inc. ATTN: Dr. Paul S. Gough 1048 South St. Portsmouth, NH 03801-5423	1	University of Michigan Gas Dynamics Laboratory Aerospace Engineering Building ATTN: Prof. Gerard M. Faeth Ann Arbor, MI 48109-2140
		2	University of Delaware Department of Chemistry ATTN: Mr. James Cronin Prof. Thomas Brill Newark, DE 19711